# Inviscid vortex shedding model for the clap and fling motion of insect flights

Sung-Ik Sohn*

*Department of Mathematics, Gangneung-Wonju National University, Gangneung 25457, South Korea and School of Mathematics, Korea Institute for Advanced Study, Seoul 02455, South Korea*

(Received 1 January 2018; revised manuscript received 1 July 2018; published 5 September 2018)

In this paper, we study the clap and fling motion of insect flights by applying an inviscid vortex shedding model. We describe separated vortices from the edges of two wings by vortex sheets and extend the model to the two bodies with symmetry. The model demonstrates sucking of leading edge vortices between the wings in the fling process. Remarkably, leading edge vortices move forward and backward as the wings close and open in the clap and fling process. We also calculate lift and drag coefficients of the wings. The numerical results show that the shedding rates at the edges increase at the rotational and acceleration phases of the fling process, which generate a large lift. When the full clap and fling stroke is taken, lift of the model dramatically increases at the rotational phase, which is much larger than results of Navier-Stokes simulations of low and moderate Reynolds numbers. This result suggests the use of the Weis-Fogh mechanism for larger insects flying at high Reynolds numbers.

DOI: 10.1103/PhysRevE.98.033105

## I. INTRODUCTION

The flight of insects has attracted much attention for the last few decades due to possible applications to micro-air vehicles. It has been shown that the conventional aerodynamic theory based on steady flows cannot explain the generation of large lift by small insects and unsteady aerodynamics should be considered. A fascinating unsteady flight motion of small insects is the so-called "clap and fling" mechanism, first discovered by Weis-Fogh [1] while analyzing the hovering motion of the tiny wasp *Encarsia formosa*. Clap and fling has been observed in a wide variety of insect species; for example, tiny insects include the greenhouse whitefly *Trialeurodes vaporariorium* [2], thrips [3], the parasitoid wasp *Muscidifurax raptor*, and the jewel wasp *Nasonia vitripennis* [4]. Larger insects such as moths, butterflies, and locusts also use the Weis-Fogh mechanism [3,5]. It was recently reported that the zooplanktonic sea butterfly *Limacina helicina* swims underwater in a similar way [6].

In the motion of clap and fling, the wings first *clap* together by rotating about the leading edges and then *fling* apart by rotating about the lower edges and subsequently translate away from each other. The schematic of clap and fling is illustrated in Fig. 1. Lighthill [7] described that the fling phase provides a mechanism for instantaneous generation of circulation and lift, using an inviscid potential-flow theory. The importance of Lighthill's theory is that the Weis-Fogh mechanism works even in the *ideal* fluid. Bennett [8] first conducted an experiment for fling for a very high Reynolds number and measured lift. Maxworthy [9] showed by the flow visualization experiment that two large leading edge vortices are generated during the fling process, which are due to viscous effects. The magnitude of the circulation on each wing from the experiment was substantially larger than that predicted by Lighthill. The instantaneous lift force on the wings during the fling process measured in Spedding and Maxworthy [10] was also larger than that by Lighthill. Edwards and Cheng [11] modified Lighthill's theory by adding a pair of point vortices to represent the leading edge vortices. Kolomenskiy *et al.* [12] also reconsidered Lighthill's theory to account for viscous effects.

The Weis-Fogh mechanism has been studied numerically by several authors, solving the Navier-Stokes equations. Sun and Yu [13] showed that in the fling process, a large lift is generated in the rotation phase and in the beginning of the translation phase. Miller and Peskin [14] calculated the full clap and fling stroke for a range of the Reynolds number between 8 and 128 and showed that lift enhancement of clap and fling is larger for lower Reynolds numbers, which suggests the efficient use of this mechanism for small insects. Kolomenskiy *et al.* [15] conducted full three-dimensional simulations for the fling motion and found that three-dimensional effects become important after the wings move farther than one chord length apart. We note that most of these numerical studies focus on the regimes of small and moderate Reynolds numbers. However, the structure of leading and trailing edge vortices differs considerably between small and large Reynolds numbers, which was demonstrated by Maxworthy's experiment [9] for the fling process. Birch *et al.* [16] also showed from experiments for flapping wings that the flow structure of the leading edge vortex significantly differs between small and large Reynolds numbers. To the author's knowledge, the Weis-Fogh mechanism at high Reynolds numbers has not been studied thoroughly.

In this paper, we study the clap and fling motion by applying an inviscid vortex shedding model in two dimensions. Separated vortices from the edges of the wings are described by vortex sheets in this model, and their evolutions are calculated numerically. Our model may be viewed as an extension of the single-vortex model by Edwards and Cheng and is mainly applicable to high Reynolds number flows. Our model thus is

*sohnsi@gwnu.ac.kr

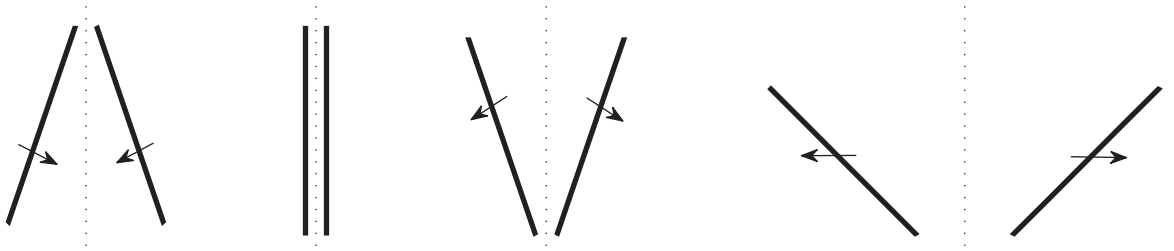

FIG. 1. Schematic for the clap and fling motion. The wings *clap* together by rotating about the leading edges and then *fling* apart by rotating about the lower edges and subsequently translate away from each other.

in connection with the use of clap and fling by the larger insects mentioned above. The purpose of this study is to quantify lift-enhancing effects of the Weis-Fogh mechanism at high Reynolds numbers.

The vortex sheet model for separated vortices from a solid body was first studied by Nitsche and Krasny [17]. A key issue in this approach is to ensure the boundedness of the velocity field at the edge of a body, i.e., the unsteady Kutta condition. Jones [18] developed a model for vortex shedding from a rigid plate, imposing the Kutta condition analytically. The vortex sheet model then has been extended and applied to various problems of vortex-body interactions: falling cards [19,20], a deforming body with a prescribed motion [21], and the flapping flag instability [22]. The vortex sheet model has been studied to demonstrate qualitative features of the vortex shedding process, but quantitative aspects such as lift and drag have never been taken into account. In this paper, we extend the model to the two bodies with symmetry and calculate lift and drag coefficients of the wings to examine whether lift is enhanced by the Weis-Fogh mechanism at high Reynolds numbers.

In Sec. II, we describe the problem setting of the clap and fling motion. We present the inviscid vortex shedding model in Sec. III and the numerical method in Sec. IV. The numerical method is validated for an unsteady motion of a plate as a test problem in Sec. V. Numerical results for the the fling half-stroke and the full clap and fling stroke are presented in Secs. VI and VII, respectively. Section VIII gives conclusions.

## II. PROBLEM DESCRIPTION

We describe the clap and fling motion of insects. We basically follow the problem setting in the computational work by Miller and Peskin [14]. In the clap and fling motion, the wings of the chord length $L$ are translated towards each other from rest at a constant angle of attack. Near the end of the initial half-stroke, the wings rotate with respect to the leading edge and are nearly clapped. The distance of $L/5$ is left between the two wings, which is slightly larger than one used in Miller and Peskin [14]. This half-stroke is called the upstroke, and the second half-stroke is called the downstroke. At the beginning of the downstroke, the wings rotate with respect to the trailing edge and then translate away from each other. The translational phase of the downstroke begins before the rotational phase finishes.

More precisely, the translational velocity during the acceleration phase of the right wing is given by

$$V(t') = -\frac{1}{2}V_{\max}\left\{1+\cos\left[\pi+\frac{\pi(t'-t'_{\rm acc})}{\Delta t'_{\rm acc}}\right]\right\}, \quad (1)$$

with $t' = tV_{\max}/L$, where $V_{\max}$ is the maximum translational velocity during the stroke, $V(t')$ is the translational velocity at dimensionless time $t'$, $t$ is the actual time, $t'_{\rm acc}$ is the dimensionless time when translational acceleration begins, and $\Delta t'_{\rm acc}$ is the dimensionless duration of translational acceleration. The left wing is the mirror image of the right wing with respect to the vertical axis at all times. After acceleration, the wing translates with the constant speed $-V_{\max}$. The translational velocity during deceleration is given by

$$V(t') = \frac{1}{2}V_{\max}\left\{-1+\cos\left[\pi+\frac{\pi(t'-t'_{\rm dec})}{\Delta t'_{\rm dec}}\right]\right\}, \quad (2)$$

where $t'_{\rm dec}$ is the dimensionless time when translational deceleration begins, and $\Delta t'_{\rm dec}$ is the dimensionless duration of translational deceleration. In the computation, the dimensionless durations of the clap and fling strokes are taken as 5.4 and 3.6, respectively. This gives a translational distance of 3.23 chord lengths during the clap stroke. The dimensionless duration of a fling-only stroke is taken as 5.4. The parameters $\Delta t'_{\rm acc}$ and $\Delta t'_{\rm dec}$ are set to 1.3, and $t'_{\rm acc}$ and $t'_{\rm dec}$ are taken so as to begin translational acceleration and end translational acceleration at $5.4 \pm 0.87$, respectively. (In the initial acceleration, $t'_{\rm acc} = 0$.) Figure 2 plots the dimensionless translational and angular velocities of the wing with respect to dimensionless time for a clap and fling stroke. The motion for $0 \leqslant t' \leqslant 9$ is used for the clap and fling simulation. For the fling simulation, the

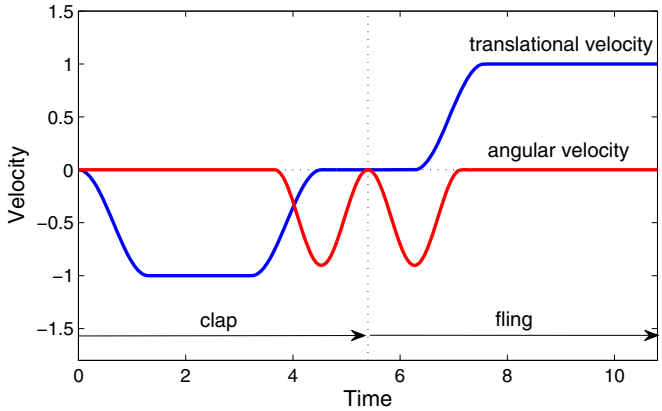


FIG. 2. Dimensionless translational and angular velocities of the wing with respect to dimensionless time for a clap and fling stroke. The motion for $0 \leqslant t' \leqslant 9$ are used for the clap and fling simulation. For the fling simulation, the translational and angular velocities follow the second half of the curves.

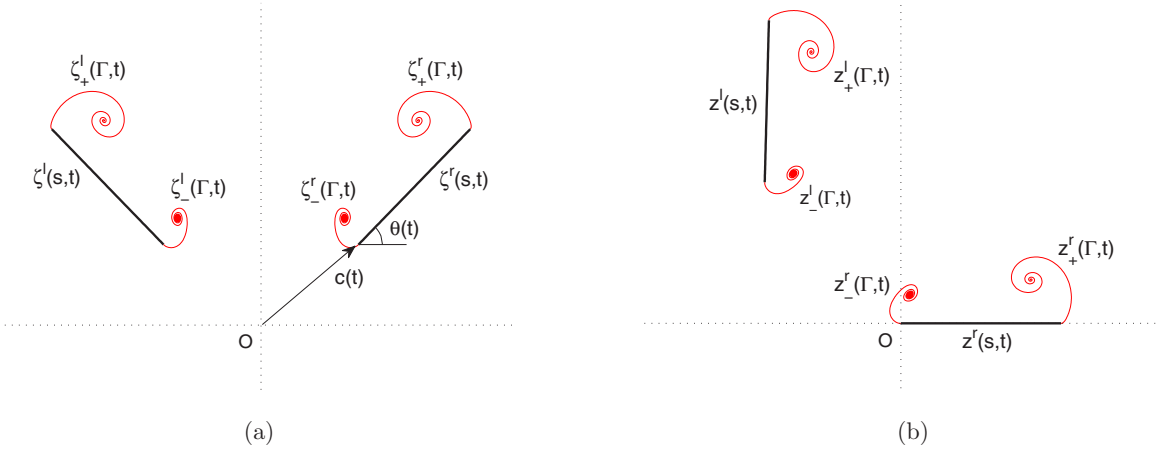


FIG. 3. Schematic of vortex shedding by the clap and fling motion: (a) laboratory frame and (b) body frame.

translational and angular velocities follow the second half of the curves.

Let us define $\theta$ as the angle of the right wing relative to the horizontal axis, assuming the origin as the trailing (leading) edge of the wing for the fling (clap) stroke. In all the fling motions, the wings rotate from $\theta = \pi/2$ to $\theta = \pi/4$ at the beginning of the downstroke, and after rotation, the angle is fixed to $\theta = \pi/4$ until the end of the stroke. In the full clap and fling motion, the wings translate with $\theta = -\pi/4$ during the upstroke and rotate to $\theta = -\pi/2$ at the end of the upstroke. The downstroke follows the same as the fling motion. The angular velocity of the right wing during the rotational phase at the end of the upstroke is given by

$$\omega(t') = -\frac{\Delta\theta\ V_{\max}}{\Delta t'_{\rm rot} L}\left[1 - \cos\left(2\pi\frac{t' - t'_{\rm rot}}{\Delta t'_{\rm rot}}\right)\right], \qquad (3)$$

where $t'_{\rm rot}$ is the dimensionless time that the wing rotation begins, $\Delta t'_{\rm rot}$ is the dimensionless duration of the rotational phase, and $\Delta\theta$ is the total angle of rotation. $\Delta\theta$ is set to $\pi/4$ and $\Delta t'_{\rm rot}$ is set to 1.74. Rotation at the beginning of the downstroke is given similarly.

## III. VORTEX SHEDDING MODEL

We consider the two-dimensional incompressible flow of an inviscid fluid generated by the unsteady motion of two rigid plates of zero thickness. We assume that the plates are symmetric with respect to the vertical axis, and free vortex sheets are separated from the edges of the plates. The flat plates are also regarded as bound vortex sheets. Recall that a vortex sheet is a surface across which the tangential velocity is discontinuous. The vortex shedding model for general two (or multiple) plates has not been studied, to the author's knowledge, and its solution procedure is not known. Nonetheless, in the clap-fling motion, one can solve the equations by using the flow characteristic, i.e., symmetry of the flow.

The scales of the flow are nondimensionalized by taking the characteristic length and velocity as the chord length of the plate $L$ and the maximum translational velocity $V_{\max}$, as in the previous section. Therefore, the dimensionless chord length and maximum translation velocity of the plate are 1. The primes in the variables are suppressed for short notation.

Figure 3(a) illustrates the flow of vortex shedding of the fling motion in a laboratory frame of reference. In the right-hand side, the plate $\zeta^r(s,t)$ is parameterized by the arc length $s$, $0 \leqslant s \leqslant 1$, and the free vortex sheets are denoted by $\zeta^r_\pm(\Gamma,t)$ where $\Gamma$ represents the circulation as a Lagrangian parameter. We use the superscripts $r$ and $l$ to distinguish the right and left. $\Gamma^r_+(t)$ and $\Gamma^r_-(t)$ denotes the total circulation of the free vortex sheets emanating at the edges of the right plate. $\Gamma^l_+(t)$ and $\Gamma^l_-(t)$ are similarly defined and have the negative values of $\Gamma^r_+(t)$ and $\Gamma^r_-(t)$, respectively, by symmetry. The plate and free vortex sheets in the left are defined as the image locations with respect to the vertical axis, which are denoted by $\zeta^l(s,t)$ and $\zeta^l_\pm(\Gamma,t)$ respectively. The two plates are then expressed by

$$\zeta^r(s,t) = c(t) + se^{i\theta}, \qquad \zeta^l(s,t) = -c(t) - se^{-i\theta} \qquad (4)$$

for $0 \leqslant s \leqslant 1$, where $c(t)$ denotes the location of the trailing (leading) edge of the right plate in the fling (clap) stroke and $\theta(t)$ denotes the same as previously defined.

We introduce the body frame of reference with respect to the right plate; see Fig. 3(b). The laboratory frame $\zeta^r(s,t)$ is related to the body frame parametrization $z^r(s,t) = s$ through $s = (\zeta^r(s,t) - c(t))e^{-i\theta}$. We denote $z^r_\pm(\Gamma,t)$ and $z^l_\pm(\Gamma,t)$ as the position of the free vortex sheets $\zeta^r_\pm(\Gamma,t)$ and $\zeta^l_\pm(\Gamma,t)$ in the body frame, respectively, where they are given by $z^j_\pm(\Gamma,t) = (\zeta^j_\pm(s,t) - c(t))e^{-i\theta}$ for $j = r$ and $l$. The left plate in the body frame is given by $z^l(s,t) = -(2c(t) + se^{-i\theta})e^{-i\theta}$.

### A. Equations for free vortex sheets

The evolution of the free vortex sheets is described by the Birkhoff-Rott equation:

$$\frac{\partial z^r_\pm}{\partial t}(\Gamma,t) = \bar{w}(z^r_\pm(\Gamma,t),t) - \dot{c}(t)e^{-i\theta} - i\dot{\theta}(t)z^r_\pm(s,t), \qquad (5)$$

where the bar represents the complex conjugate of the velocity field in the body frame of reference and a dot represents time derivative. We define the vortex sheet strength $\gamma(s,t)$ as the jump in the tangential velocity across the bound vortex sheet.

The velocity $w(z,t)$ is then expressed as the boundary integral

$$w(z,t) = \frac{1}{2\pi i}\int_0^1 \frac{\gamma^r(\lambda,t)}{\lambda - z}d\lambda + \frac{1}{2\pi i}\int_0^1 \frac{\gamma^l(\lambda,t)}{z^l(\lambda,t)-z}d\lambda - \frac{1}{2\pi i}\left[\int_0^{\Gamma^r_\pm(t)} \frac{d\Lambda}{z^r_\pm(\Lambda,t)-z}\right]^+_- - \frac{1}{2\pi i}\left[\int_0^{\Gamma^l_\pm(t)} \frac{d\Lambda}{z^l_\pm(\Lambda,t)-z}\right]^+_-, \quad (6)$$

where the square bracket denotes a difference, $[\alpha_\pm] = \alpha_+ - \alpha_-$. Since $\gamma^l(s,t) = -\gamma^r(s,t)$ and $\Gamma^l_\pm(t) = -\Gamma^r_\pm(t)$, we have

$$w(z,t) = \frac{1}{2\pi i}\int_0^1 \frac{\gamma^r(\lambda,t)}{\lambda - z}d\lambda - \frac{1}{2\pi i}\int_0^1 \frac{\gamma^r(\lambda,t)}{z^l(\lambda,t)-z}d\lambda - \frac{1}{2\pi i}\left[\int_0^{\Gamma^r_\pm(t)} \frac{d\Lambda}{z^r_\pm(\Lambda,t)-z}\right]^+_- + \frac{1}{2\pi i}\left[\int_0^{\Gamma^r_\pm(t)} \frac{d\Lambda}{z^l_\pm(\Lambda,t)-z}\right]^+_-. \quad (7)$$

The first and second integrals in Eq. (7) represent a contribution from the bound vortex sheets, and the third and fourth integrals represent a contribution from the free vortex sheets. The bound vortex sheet strength $\gamma^r(s,t)$ and the edge circulations $\Gamma^r_\pm(t)$ are not known beforehand and should be determined as part of the solution.

### B. Equations for bound vortex sheet strength

To find the bound vortex sheet strength and edge circulations, we apply the kinematic condition and the unsteady Kutta condition. The unsteady Kutta condition is imposed to ensure that the velocity on the bound vortex sheet remains bounded [18,21].

The kinematic condition implies that the normal component of the fluid velocity on either side of the body should be the same as the normal component of the body's velocity. Following Jones [18], one can find that the kinematic condition gives the following equation:

$$\frac{1}{\pi}\int_0^1 \frac{\gamma^r(\lambda,t)}{\lambda - s}d\lambda + \mathrm{Re}\left[\frac{1}{\pi}\int_0^1 \frac{\gamma^l(\lambda,t)}{z^l(\lambda,t)-s}d\lambda\right] = f(s,t), \quad \text{for} \quad s\in[0,1]. \quad (8)$$

The right-hand side takes the form

$$f(s,t) = 2v(s,t) + \mathrm{Re}\left\{\frac{1}{\pi}\left[\int_0^{\Gamma^r_\pm(t)} \frac{d\Lambda}{z^r_\pm(\Lambda,t)-s}\right]^+_- + \frac{1}{\pi}\left[\int_0^{\Gamma^l_\pm(t)} \frac{d\Lambda}{z^l_\pm(\Lambda,t)-s}\right]^+_-\right\}, \quad (9)$$

where $v(s,t)$ is the normal component of the velocity of the right plate and is given by

$$v(s,t) = \mathrm{Im}\{\dot{c}(t)e^{-i\theta}\} + \dot{\theta}(t)s. \quad (10)$$

Using the symmetry again, Eq. (8) is written as the singular Fredholm integral equation of the first kind for the bound vortex sheet strength $\gamma^r(s,t)$,

$$\frac{1}{\pi}\int_0^1 \frac{\gamma^r(\lambda,t)}{\lambda - s}d\lambda + \mathrm{Re}\left\{\frac{1}{\pi}\int_0^1 M(s;\lambda,t)\gamma^r(\lambda,t)\,d\lambda\right\} = f(s,t), \quad \text{for} \quad s\in[0,1], \quad (11)$$

where the kernel $M(s;\lambda,t)$ and $f(s,t)$ are given by

$$M(s;\lambda,t) = \frac{1}{z^l(\lambda,t)-s}, \quad (12)$$

$$f(s,t) = 2v(s,t) + \mathrm{Re}\left\{\frac{1}{\pi}\left[\int_0^{\Gamma^r_\pm(t)} \frac{d\Lambda}{z^r_\pm(\Lambda,t)-s}\right]^+_- - \frac{1}{\pi}\left[\int_0^{\Gamma^r_\pm(t)} \frac{d\Lambda}{z^l_\pm(\Lambda,t)-s}\right]^+_-\right\}. \quad (13)$$

The integral equation (11) cannot be solved analytically, while in the case of a single rigid plate, the solution is expressed explicitly [18]. However, Eq. (11) is of a similar form as that for a deforming body by Shukla and Eldredge [21]. Since the only difference is the kernel $M(s;\lambda,t)$ and an additional term in $f(s,t)$, we follow the similar procedure as them. For functions $\gamma^r(s,t)$ and $f(s,t)$ satisfying Hölder continuity on $s\in[0,1]$, and $M(s;\lambda,t)$ Hölder continuous with respect to both $s$ and $\lambda$ over the same interval, the integral equation (11) can be converted to a Fredholm equation of the second kind,

$$\gamma^r(s,t) + \int_0^1 N(s;\lambda,t)\gamma^r(\lambda,t)\,d\lambda = F(s,t), \quad (14)$$

with a constraint

$$\frac{1}{\pi}\int_0^1\left[\int_0^1 \frac{M(s;\lambda,t)}{\sqrt{s(1-s)}}ds\right]\gamma^r(\lambda,t)\,d\lambda = \int_0^1 \frac{f(\lambda,t)}{\sqrt{\lambda(1-\lambda)}}d\lambda, \quad (15)$$

where

$$N(s;\lambda,t) = -\frac{1}{\pi^2}\int_0^1 \sqrt{\frac{s(1-s)}{\zeta(1-\zeta)}}\frac{M(\zeta;\lambda,t)}{\zeta - s}d\zeta, \quad (16)$$

$$F(s,t) = -\frac{1}{\pi}\int_0^1 \sqrt{\frac{s(1-s)}{\lambda(1-\lambda)}}\frac{f(\lambda,t)}{\lambda - s}d\lambda. \quad (17)$$

We note that $f(s,t)$ given by Eq. (13) has logarithmic singularities at the ends $s=0$ and 1. The free vortex sheets, however, need a regularization, and this ensures that the regularized function satisfies Hölder continuity at the ends and also gives $\gamma^r(s=0,t)=0$ and $\gamma^r(s=1,t)=0$. In order to close the equations, we apply Kelvin's circulation theorem,

$$\int_0^1 \gamma^r(s,t)\,ds = \Gamma^r_+(t) - \Gamma^r_-(t). \quad (18)$$

Then Eqs. (14), (15), and (18) give a system of equations for the unknowns $\gamma^r(s,t)$, $\Gamma^r_+(t)$, and $\Gamma^r_-(t)$.

### C. Force on the body

The only force acting on the body is the normal force which acts with the pressure difference across the two sides of the body, since the fluid is inviscid. The pressure difference across the two sides of the bound vortex sheet is given by

$$[p^r(s,t)] = -\frac{d\Gamma^r}{dt}(s,t) - \gamma^r(s,t)[\mu^r(s,t) - \tau^r(t)], \quad (19)$$

where $\mu^r(s,t)$ is the tangential component of the average of the fluid velocities on either side of the body, which takes the form

$$\mu^r(s,t) = \mathrm{Im}\left\{-\frac{1}{2\pi}\int_0^1 \frac{\gamma^r(\lambda,t)}{z^l(\lambda,t)-s}\,d\lambda - \frac{1}{2\pi}\left[\int_0^{\Gamma^r_\pm(t)} \frac{d\Lambda}{z^r_\pm(\Lambda,t)-s}\right]_-^+ + \frac{1}{2\pi}\left[\int_0^{\Gamma^r_\pm(t)} \frac{d\Lambda}{z^l_\pm(\Lambda,t)-s}\right]_-^+\right\}, \quad (20)$$

and $\tau^r(t) = \mathrm{Re}\{\dot{c}(t)e^{-i\theta(t)}\}$ is the tangential component of the velocity of the body. The circulation on the body is expressed as

$$\Gamma^r(s,t) = \Gamma^r_-(t) + \int_0^s \gamma^r(\lambda,t)\,d\lambda. \quad (21)$$

Note that the pressure difference across the free vortex sheet is zero. The total normal force on the right body is expressed as

$$\mathbb{F}(t) = -e^{-i\theta(t)}\int_0^1 [p^r(\lambda,t)]\,d\lambda. \quad (22)$$

The lift and drag force follow from the total normal force $\mathbb{F}(t)$. Conventionally by scaling by $\rho V_{\max}^2 L/2$, the lift and drag coefficients are defined as

$$C_L = \frac{2F_L}{\rho V_{\max}^2 L} \quad \text{and} \quad C_D = \frac{2F_D}{\rho V_{\max}^2 L}, \quad (23)$$

where $F_L$ is the lift force per unit length, $F_D$ is the drag force per unit length, and $\rho$ is the density of the fluid.

## IV. NUMERICAL METHOD

### A. Regularization of the equations

The vortex sheet evolution suffers from the Kelvin-Helmholtz instability for all the disturbance wave numbers. It is well known that in a free shear flow, the vortex sheet develops a singularity at finite time [23]. Numerical computations for the vortex sheet break down when the singularity appears. The singularity could be suppressed by giving a numerical smoothing or physical effects such as viscous diffusion, finite thickness, or surface tension. The most common regularization for a vortex sheet is the vortex blob model in which the singular kernel $K(z) = 1/z$ is replaced by a smoothed kernel [24,25]. A widely used blob regularization is to give a constant parameter $\delta = \delta_0$ in the kernel,

$$K_\delta(z) = \frac{\bar{z}}{z\bar{z} + \delta^2}. \quad (24)$$

Note that the blob regularization should not be applied to the bound vortex sheet, since such regularization makes the equation ill-posed. Thus there is a jump in the regularization parameter at the edges of the bound vortex sheet when the uniform regularization is applied. The jump of the regularization parameter often yields oscillations in the solution at an early time. To avoid the oscillations, a small value of $\delta_0$ should be used, but then the computation becomes expensive, because of high resolution of spiral cores.

Alben [26] proposed a tapered smoothing using nonuniform $\delta(s)$, in order to reconcile the regularization of the free vortex sheet with the absence of regularization on the bound vortex sheet. In this approach, $\delta(s)$ gradually decreases to 0 as the arc-length $s$ approaches the edges of the bound vortex sheet. For the free vortex sheet separated from the edge of the body, $\delta(s)$ is given by

$$\delta(s) = \delta_0(1 - e^{-s(\Gamma)^2/\epsilon^2}). \quad (25)$$

The parameter $\epsilon$ gives the scale over which $\delta(s)$ goes to zero. We have found that the tapered regularization (25) is unstable at certain situations. In order to enhance the stability, we introduce another small parameter $\tau$ and modify the nonuniform regularization (25) to the following form:

$$\delta(s) = \delta_0[1 - (1-\tau)e^{-s(\Gamma)^2/\epsilon^2}]. \quad (26)$$

This parameter $\delta(s)$ decreases to $\delta_0\tau$ as $s \to 0$. For small $s$, it behaves as $\delta(s) \sim \delta_0[\tau + (1-\tau)s^2/\epsilon^2]$ and thus decreases with a similar rate with Eq. (25). The modified nonuniform regularization (26) calculates separated free vortex sheets efficiently and stably. In our simulations, the parameters are set to $\epsilon = 2\delta_0$ and $\tau = 0.05$.

With the blob regularization, the velocity field $w_\delta(z,t)$ takes the form

$$w_\delta(z,t) = \frac{1}{2\pi i}\int_0^1 \frac{\gamma^r(\lambda,t)}{\lambda - z}\,d\lambda - \frac{1}{2\pi i}\int_0^1 \frac{\gamma^r(\lambda,t)}{z^l(\lambda,t)-z}\,d\lambda - \frac{1}{2\pi i}\left\{\int_0^{\Gamma^r_\pm(t)} K_\delta[z^r_\pm(\Lambda,t)-z]\,d\Lambda\right\}_-^+ + \frac{1}{2\pi i}\left\{\int_0^{\Gamma^r_\pm(t)} K_\delta[z^l_\pm(\Lambda,t)-z]\,d\Lambda\right\}_-^+. \quad (27)$$

The regularized equation for the evolution of the free vortex sheets is given by

$$\frac{\partial z^r_\pm}{\partial t}(\Gamma,t) = \bar{w}_\delta(z^r_\pm(\Gamma,t),t) - \dot{c}(t)e^{-i\theta} - i\dot{\theta}(t)z^r_\pm(s,t), \quad (28)$$

where $\gamma^r(s,t)$, $\Gamma^r_+(t)$, and $\Gamma^r_-(t)$ are determined from the following equations:

$$\begin{aligned} &\gamma^r(s,t) + \int_0^1 N(s;\lambda,t)\gamma^r(\lambda,t)\,d\lambda \\ &\quad = F_\delta(s,t), \quad \text{for } s \in [-1,1], \\ &\frac{1}{\pi}\int_0^1 \left\{\int_0^1 \frac{M(s;\lambda,t)}{\sqrt{s(1-s)}}\,ds\right\}\gamma^r(\lambda,t)\,d\lambda \\ &\quad = \int_0^1 \frac{f_\delta(\lambda,t)}{\sqrt{\lambda(1-\lambda)}}\,d\lambda, \\ &\int_0^1 \gamma^r(s,t)\,ds = \Gamma^r_+(t) - \Gamma^r_-(t). \end{aligned} \quad (29)$$

Here $f_\delta$ and $F_\delta$ are given by

$$f_\delta(s,t) = 2\nu(s,t) + \mathrm{Re}\left(\frac{1}{\pi}\left\{\int_0^{\Gamma^r_\pm(t)} K_\delta[z^r_\pm(\Lambda,t) - s]\, d\Lambda\right\}^+_- - \frac{1}{\pi}\left\{\int_0^{\Gamma^r_\pm(t)} K_\delta[z^l_\pm(\Lambda,t) - s]\, d\Lambda\right\}^+_-\right),$$

$$F_\delta(s,t) = -\frac{1}{\pi}\int_0^1 \sqrt{\frac{s(1-s)}{\lambda(1-\lambda)}}\,\frac{f_\delta(\lambda,t)}{\lambda - s}\, d\lambda.$$

### B. Discretization and time integration

For the discretization of the vortex sheets and the time integration of the equations, we follow a similar procedure as Shukla and Eldredge [21] and here briefly summarize it. We discretize the free and bound vortex sheets, on the right, by $N$ Lagrangian point vortices. Using the circulation $\Gamma$ as a Lagrangian variable, we denote the locations of the free vortex sheets by $z^r_j = z^r_\pm(\Gamma_j, t)$ for $1 \leqslant j \leqslant P-1$ and $Q+1 \leqslant j \leqslant N$. We use the integers $P$ and $Q$ to denote the Lagrangian indices of the leading and trailing edges of the bound vortex sheet, respectively. The bound vortex sheet is discretized by using Gauss-Lobatto collocation nodes, which are given by

$$s_j = \frac{1}{2}\left\{1 - \cos\left[\frac{\pi(j-P)}{Q-P}\right]\right\}, \qquad P \leqslant j \leqslant Q. \quad (30)$$

The edge circulations are given by $\Gamma^r_P = \Gamma^r_+(t)$ and $\Gamma^r_Q = \Gamma^r_-(t)$. After discretization, Eq. (29) becomes a system of linear equation for the unknowns $\Gamma^r_P$, $\Gamma^r_Q$, and $\gamma^r_j$, $P+1 \leqslant j \leqslant Q-1$, where $\gamma^r_j$ represents the discrete approximation of the bound vortex sheet strength. (Recall $\gamma^r_P = \gamma^r_Q = 0$.) In Eq. (29), the approximation of $N(s;\lambda,t)$, $F_\delta(s,t)$, and the second equation involve the integrands with square root singularities at the ends. Special numerical techniques are applied to calculate these quantities with high accuracy. Details of these techniques can be found in the appendix of Ref. [21].

Once determining $\Gamma^r_P$, $\Gamma^r_Q$, and $\gamma^r_j$ by solving the linear equation using the Gauss elimination, we calculate the right-hand side of Eq. (28), for time advancing of the free vortex sheets. In Eq. (27), the integrations over the free vortex sheets are approximated by the trapezoidal rule, while the integrations for the bound vortex sheets are obtained by the Clenshaw-Curtis quadrature, which is spectrally accurate. We employ the classical fourth-order Runge-Kutta method for time integration of Eq. (28). The two new point vortices are released from the edges of the right and left bodies at each time step. The free vortex sheets lack resolution at late times, due to the nonuniform distribution of point vortices. To handle it, an adaptive point insertion procedure is applied to maintain the resolution of the free vortex sheets. The third-order local polynomial interpolation is used to insert points whenever the distance between two consecutive points exceeds a given threshold.

The solution procedure of the equations requires initial conditions at time $t_1 > 0$. One may use the self-similar solution of the free vortex sheet separated from a plate for the initial conditions [18]. Two starting point vorticies with zero circulation $\Gamma^r_1 = \Gamma^r_N = 0$ are placed initially, and their locations $z^r_1$ and $z^r_N$ are given by the small-time asymptotic expansion of the self-similar solution. The initial estimates for the edge circulation $\Gamma^r_P$ and $\Gamma^r_Q$ for $P = 2$ and $Q = N-1$ are also given from the self-similar solution.

Let us note a limitation of the model. The numerical procedure of vortex shedding is valid if new vortex particles separate tangentially from the body edge. In other words,

$$\mu^r_+(t) - \tau^r(t) > 0 \quad \text{and} \quad \mu^r_-(t) - \tau^r(t) < 0, \quad (31)$$

where $\mu^r_\pm(t)$ denotes the value of $\mu^r(t)$ at the body edges. This condition does not hold in some situations, e.g., if the angle of attack is small or the free vortex sheet is located close to the body [18]. This condition restricts practical application of the model, and to the author's knowledge, no remedy has yet been proposed to handle it properly.

## V. VALIDATION OF THE NUMERICAL METHOD

Before applying the numerical method described in Sec. IV to clap-fling, we test it for an unsteady motion of a single plate, which was considered in Ref. [18]. The length scale is nondimensionalized by taking the characteristic length as $L/2$, so that the dimensionless chord length of the plate is 2. This scaling applies only for this section, for validation. The motion of the plate is given by

$$c(t) = 2.5 - \frac{1}{16}\{2\log 2 + \log\cosh[8(t-2)] + \log\cosh[8(t-3)]\},$$

$$\theta(t) = \frac{\pi}{2} + \frac{\pi}{128}\{\log\cosh[8(t-2)] - \log\cosh[8(t-3)]\}.$$

The motion of the plate consists of a forward translation, followed by a smooth stop with rotation, and then a backward translation.

Figure 4 shows the vortex shedding of the unsteady motion of a plate. The uniform regularization $\delta_0 = 0.2$ is used in Fig. 4(a), and the nonuniform regularization (26) with $\delta_0 = 0.2$, $\epsilon = 2\delta_0$, and $\tau = 0.05$ is used in Fig. 4(b). The evolution of free vortex sheets in Fig. 4(a) agrees well with the result in Ref. [18]. In Fig. 4, the center positions of the first leading and trailing edge vortices in Ref. [18] are marked by circles, for comparison. In Fig. 4(b), the vortices from the nonuniform regularization evolve similarly with those from the uniform regularization in Fig. 4(a), but some differences are observed near the edges at $t = 2$ and 3, which are the effects of small regularization. In fact, the value of $\delta$ on the edges is 0.01, which is much smaller than that in Fig. 4(a). The result in Fig. 4 shows that the nonuniform regularization gives rather strong effects near the separation points but has minor influence on the free vortex sheets away from the edges. Therefore, the nonuniform regularization not only efficiently calculates the free vortex sheets, but also provides the refined solution for separation of free vortex sheets, calculating more stably.

In Fig. 5 we compare the circulations and shedding rates on the leading and trailing edges for the two cases in Fig. 4. The thick (blue) curves correspond to the uniform regularization parameter $\delta_0 = 0.2$, and the thin (red) curves correspond to the nonuniform regularization. The results of the uniform regularization $\delta_0 = 0.2$ are in good agreement with those in Ref. [18], denoted by circles, except initially. The initial

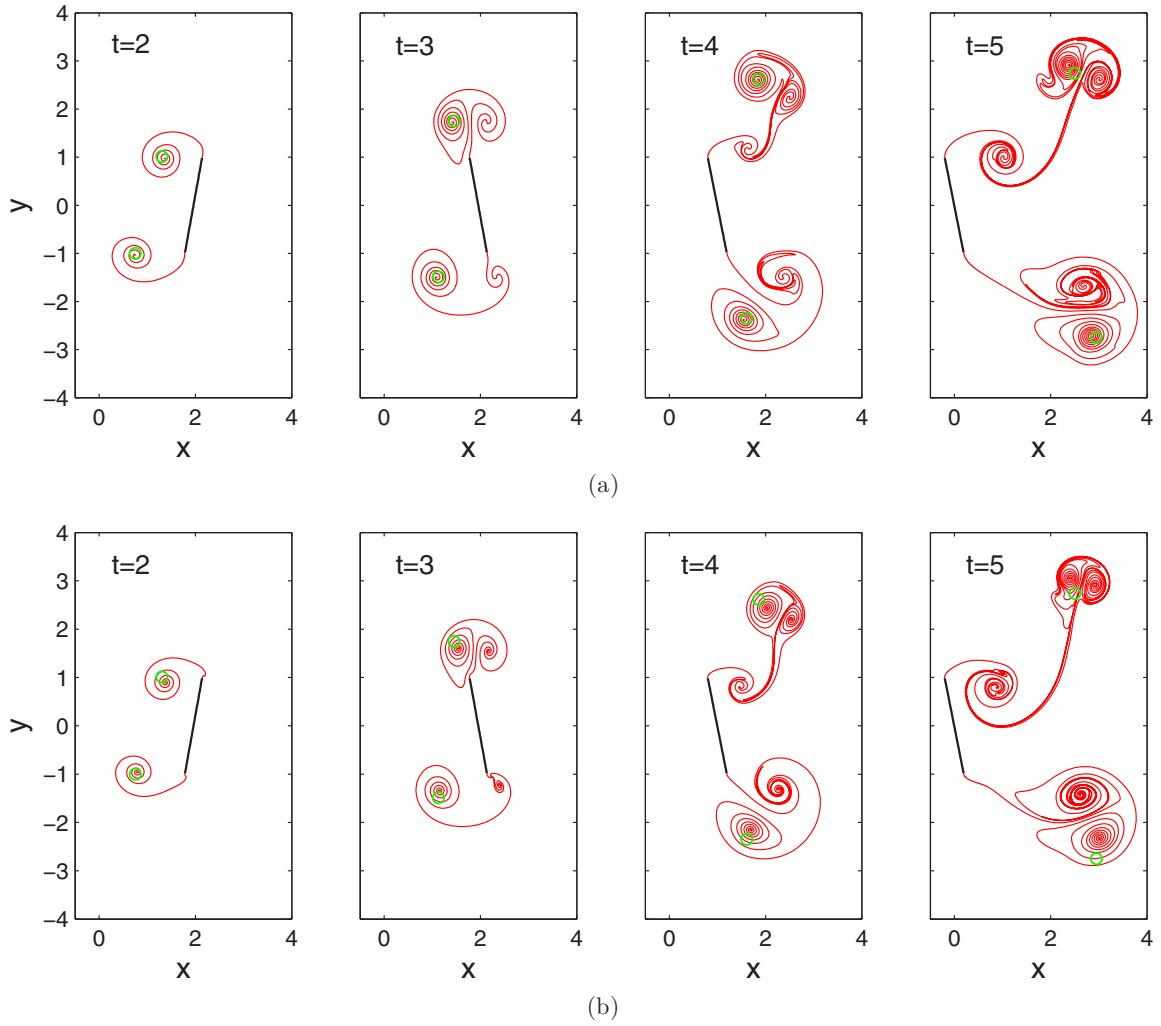


FIG. 4. Vortex shedding of the unsteady motion of a plate. (a) Uniform regularization $\delta_0 = 0.2$ and (b) nonuniform regularization $\delta(s)$ with $\delta_0 = 0.2$, $\epsilon = 2\delta_0$, and $\tau = 0.05$. The center positions of the first leading and trailing edge vortices in Ref. [18] are marked by circles (green).

difference between the two results will be due to the use of a point deletion procedure in that reference, in order to reduce the computation cost for tightly wound spirals which evolve at late times. We observe that initially, the shedding rates of the nonuniform regularization are much larger than those of the uniform regularization. In Fig. 5, the circulations of the uniform and nonuniform regularization are in agreement. The shedding rates are also overall in agreement, but the negative peaks of the nonuniform regularization are smaller in magnitude than those of the uniform regularization. The normal force on the plate for the uniform and nonuniform regularization is plotted in Fig. 6. The normal force is also in agreement, which is similar to the shedding rate.

## VI. RESULTS FOR FLING

In this section, we present numerical results for the fling motion by applying the vortex shedding model. We take the number of points as $N = 62$ initially and use the nonuniform regularization with $\delta_0 = 0.2$. Figure 7 shows the vortex shedding of the fling motion by two wings. The vortices are shed from the leading and trailing edges at early times. The leading edge vortex stays near the body and is deformed at later times, whereas the trailing edge vortex is located away from the body and rotates uniformly. At $t \geqslant 4$, we also see another vortex shedding at the trailing edge. Figure 8 plots the streamline of the fling stroke at selected times. Sixteen contour levels for the stream function are drawn for each box of Fig. 8. It clearly shows that the leading edge vortices are located near the body at $t \leqslant 3.2$. Recall that rotation and translational acceleration end at $t = 1.74$ and 2.17, respectively.

The circulation and shedding rate at the leading and trailing edges from the model are plotted in Fig. 9. The shedding rates of the leading and trailing edges grow together at early times $t < 2$ but exhibit an alternating behavior at $t > 2$. Figure 10 shows the temporal variation of lift and drag coefficients for the fling motion by two wings. The result of the Navier-Stokes (NS) simulation for Re = 128 [14] is also plotted for comparison. We observe the two peaks of the lift coefficient at early times. The first peak of lift is generated by rotational acceleration, and the second peak is produced by translational acceleration. Lift coefficient from the model drops at $2 < t < 3.4$ during translation. At this time, the shedding rate decreases at the leading edge and remains stationary at the trailing edge,

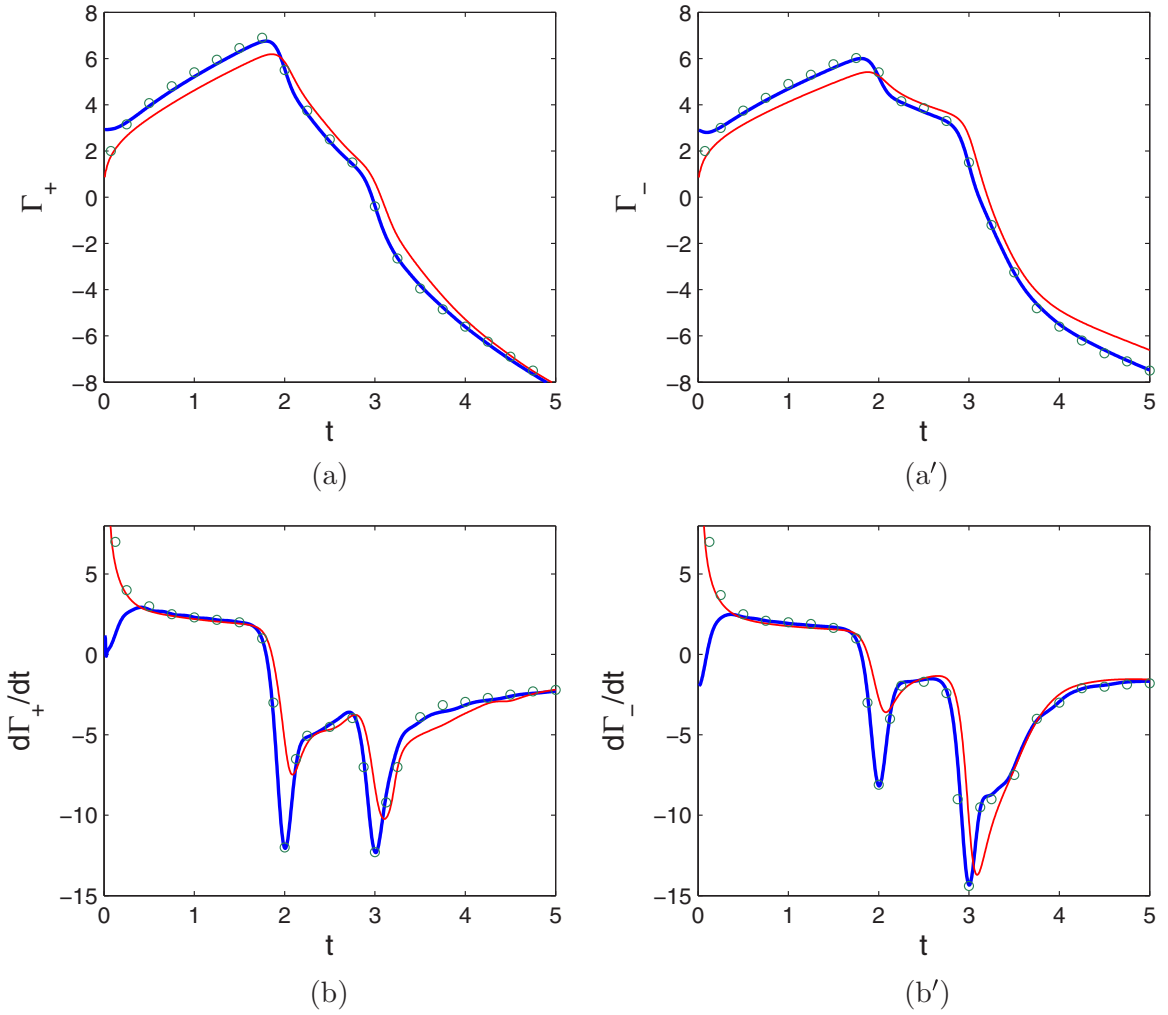


FIG. 5. Circulations and shedding rates of leading (+) and trailing (−) edges with respect to time for the unsteady motion of a plate. (a) $\Gamma_+$, (a′) $\Gamma_-$; (b) $d\Gamma_+/dt$, (b′) $d\Gamma_-/dt$. The thick (blue) curves correspond to the uniform regularization parameter $\delta_0 = 0.2$, and the thin (red) curves correspond to the nonuniform regularization $\delta(s)$. Circles denote the results in Ref. [18].

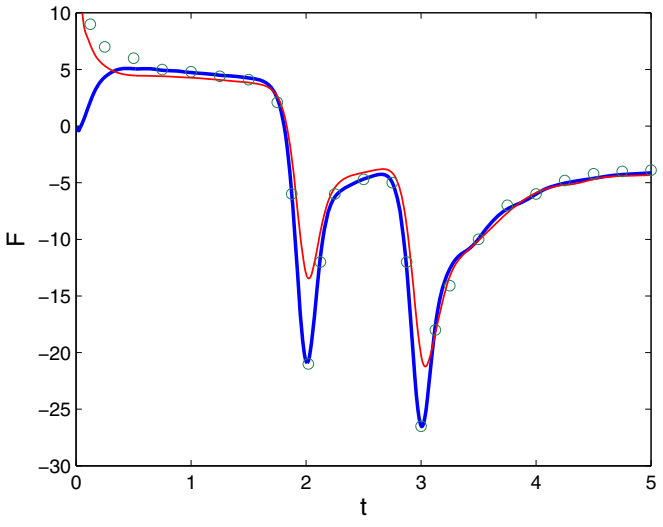


FIG. 6. Normal force for the unsteady motion of a plate. The thick (blue) and thin (red) curves correspond to the uniform regularization parameters $\delta_0 = 0.2$ and nonuniform regularization $\delta(s)$, respectively. Circles denote the result in Ref. [18].

shown in Fig. 9. The lift coefficient increases at $t > 3.4$ due to the new separating vortex at the trailing edge. Comparing with the NS simulation for Re = 128, we find that lifts of the two results vary similarly. It was shown that the first and second peaks of lift of the NS simulations decrease with the Reynolds number [14]; this trend agrees with the smaller peaks of the inviscid model than those of Re = 128. After the peaks, the lift of the inviscid model drops earlier than the NS simulation.

The drag coefficient also has the two peaks at early times, which are generated by rotational acceleration and translational acceleration, respectively. Since the first peak is larger than the second peak, drag by wing rotation is larger than that by translational acceleration. The drag coefficient of the model varies similarly with the NS simulation for Re = 128. In the NS simulations, the first and second peaks of drag decrease with the Reynolds number, and drags of Re = 32, 64, and 128 differ little at the late translation phase, which is consistent with the result in Fig. 10.

Let us compare our result with numerical and experimental studies of fling for higher Reynolds numbers. Kolomenskiy *et al.* [15] performed the three-dimensional numerical simulation for the NS equations and considered two values of

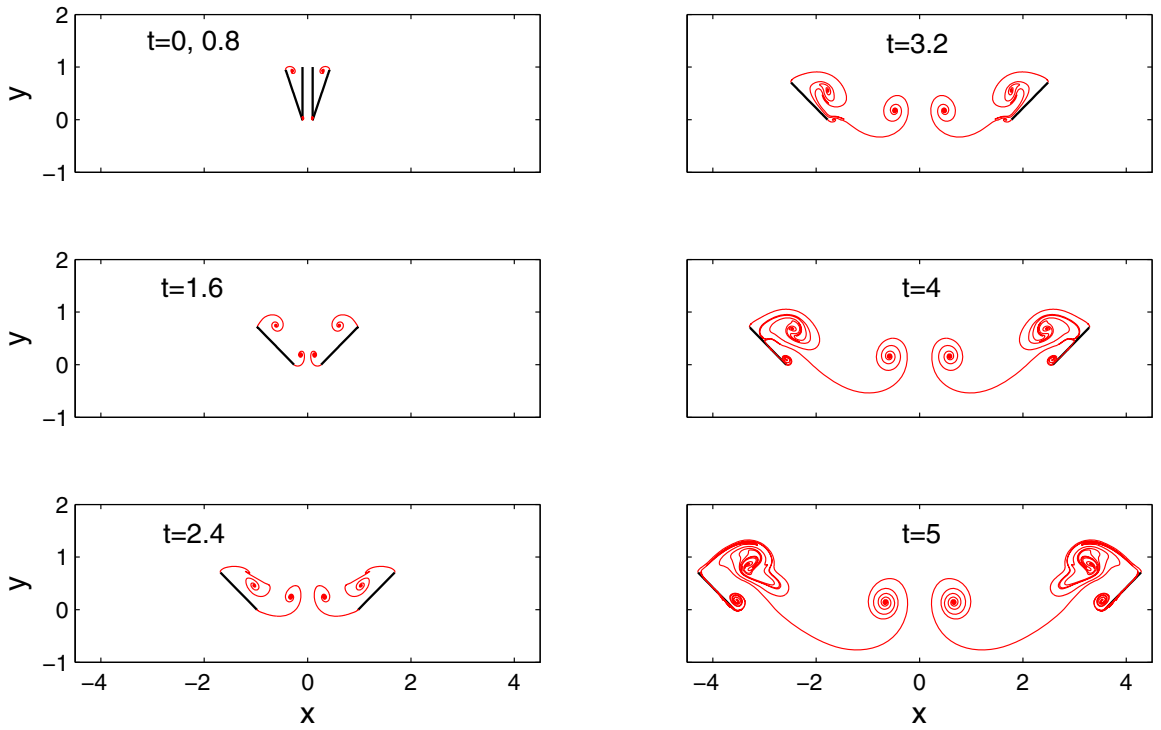


FIG. 7. Vortex shedding of the fling motion by two wings.

the Reynolds numbers, Re = 128 and 1400. For Re = 1400, they showed the formation of one large leading edge vortex and the shedding of one trailing edge vortex, radially in the middle of the wing at $t = 3.2$, which is similar to our result of Fig. 7 at the same time. They also reported that circulation on the wing for Re = 1400 is significantly smaller than that for Re = 128, at $t = 3.2$. Since smaller circulation produces a lower lifting force, it is in accordance with our result. On the other hand, Bennett [8] conducted an experiment for a very high Reynolds number, Re = 83 000, and observed the loss of lift after one and half chord of travel. In our setting, 1.5 chord of travel corresponds to time $t = 3$ and therefore is in reasonable agreement with Fig. 10 where lift drops to the minimum at $t = 3.4$. In fact, using a smaller value of the regularization parameter $\delta_0 = 0.1$ in the model, lift drops earlier, and time of its minimum coincides with $t = 3$, which is shown below in Fig. 16.

We also consider the fling motion by one wing for comparison. Figure 11 shows the vortex shedding of the one-winged fling motion. The vortices are shed from the leading and trailing

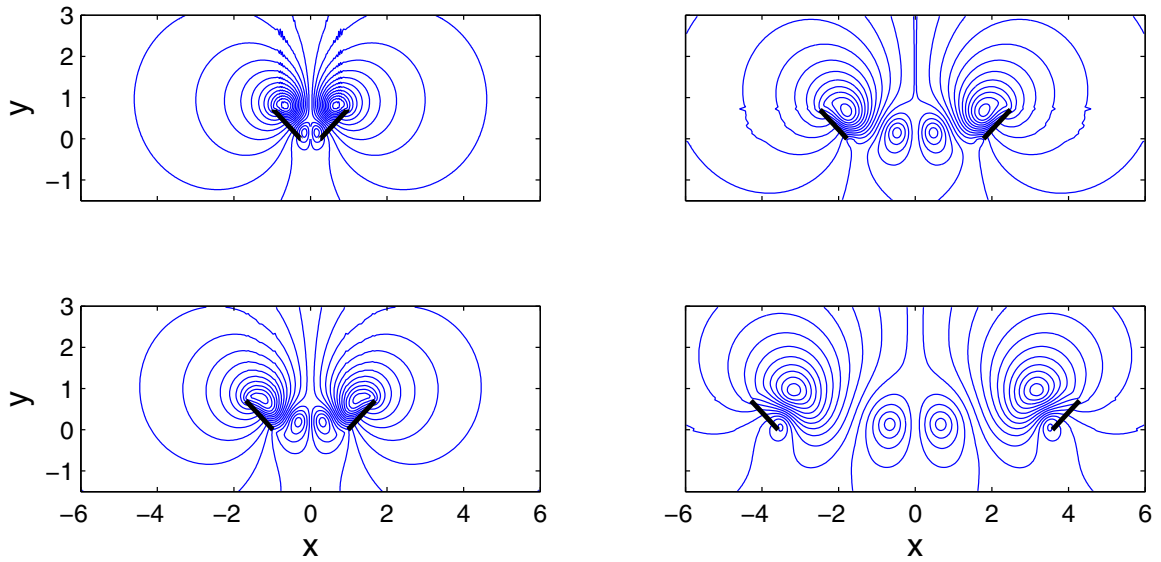


FIG. 8. Streamline of the fling motion by two wings at $t = 1.6$ (upper left), $t = 2.4$ (lower left), $t = 3.2$ (upper right), and $t = 5$ (lower right). Sixteen contour levels of the stream function are drawn for each box.

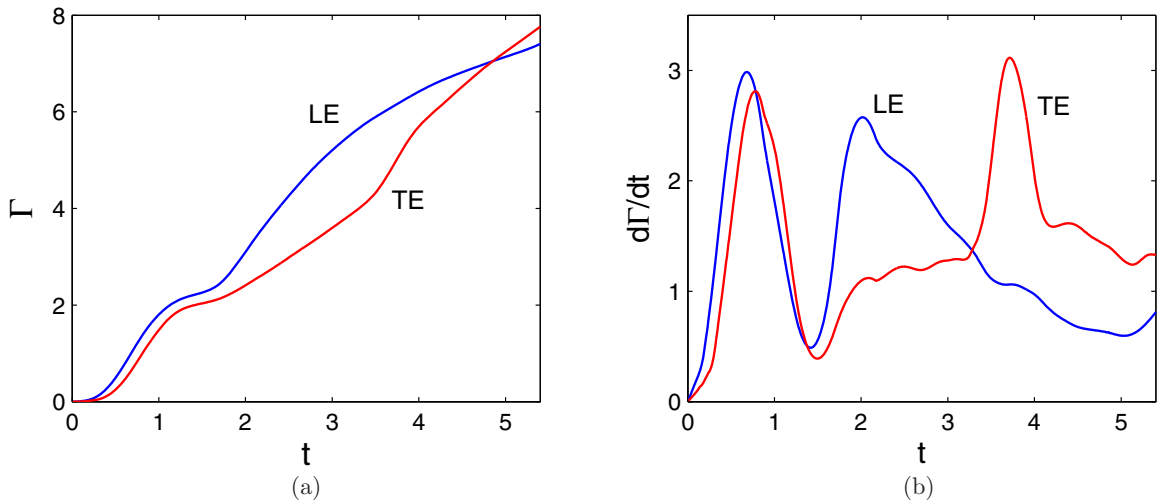


FIG. 9. (a) Edge circulation and (b) edge shedding rate with respect to time at the leading and trailing edges of the fling motion by two wings.

edges during rotation, but vortex shedding of the one-winged fling during translation has a very different pattern from that of the two-winged fling. A new leading edge vortex is separated at $t = 2.4$, whereas in the two-winged case, only one leading edge vortex of a large structure was found over all the observed times. The circulation and shedding rate at the leading and trailing edges are plotted in Fig. 12. The shedding rate at the leading edge is similar to that of the two wings, but the shedding rate at the trailing edge is considerably smaller at early times than that of the two wings and does not increase rapidly at a late time, which means a weak separated vortex.

Figure 13 shows lift and drag coefficients with respect to time for the one-winged fling motion. The result of the NS simulation for Re = 128 [14] is also plotted for comparison. We observe the two peaks of lift coefficient at early times. Similarly as the two wings, the first peak of lift is generated by rotational acceleration, and the second peak is produced by translational acceleration. Lift coefficient drops at about $t > 4$, due to no new separating vortex at the leading edge and a weak separating vortex at the trailing edge. The prediction of the model is in a qualitative agreement with the result of the NS simulation for Re = 128. Note that the lift coefficient of the NS simulation for one wing also tends to drop during translation as the Reynolds number increases [14]. Figure 13 indicates that the invicid model gives larger lifting force than the NS simulation. The drag coefficient in Fig. 13 has the two peaks at early times, but unlike the two wings, the first peak is comparable with the second one. The comparable two peaks of drag are also shown in the result of the NS simulation for Re = 128 or smaller [14]. The drag coefficient drops as the wing translates. The drag coefficient of the NS simulation is nearly constant during translation, similar to the two wings.

Let us directly compare the lift coefficient of one wing with the two wings from the model, shown in Fig. 14. The fist peak of lift of the two wings is considerably larger than that of one wing. The behavior of lift during translation is different: for the two wings, it drops and then increases, whereas for one wing, it increases slightly and then drops. The key reasons of this difference are attributed to the structure of vortices at leading and trailing edges: (1) A new leading edge vortex is

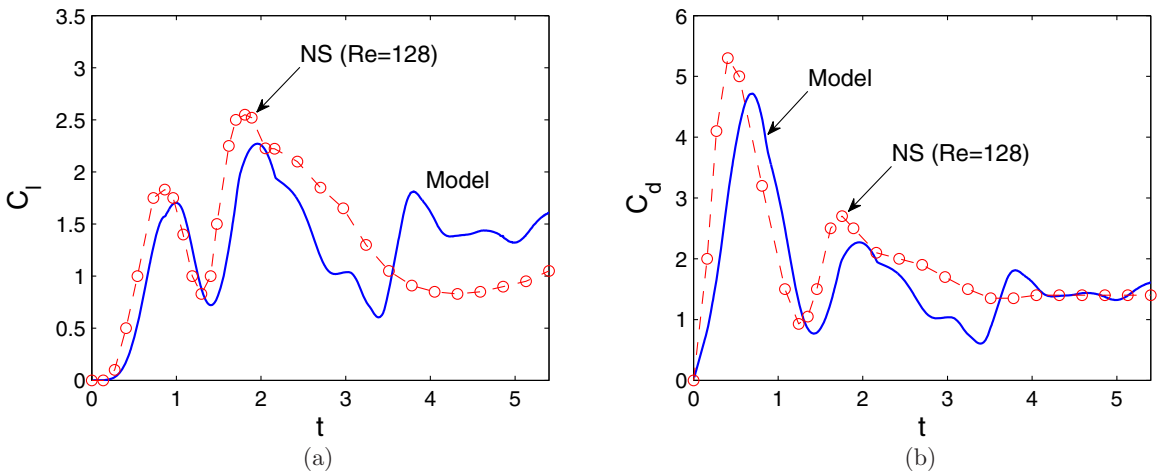


FIG. 10. (a) Lift coefficient and (b) drag coefficient for the fling motion by two wings. The curve is the prediction from the inviscid model, and the circle is the result of the Navier-Stokes simulation for Re = 128.

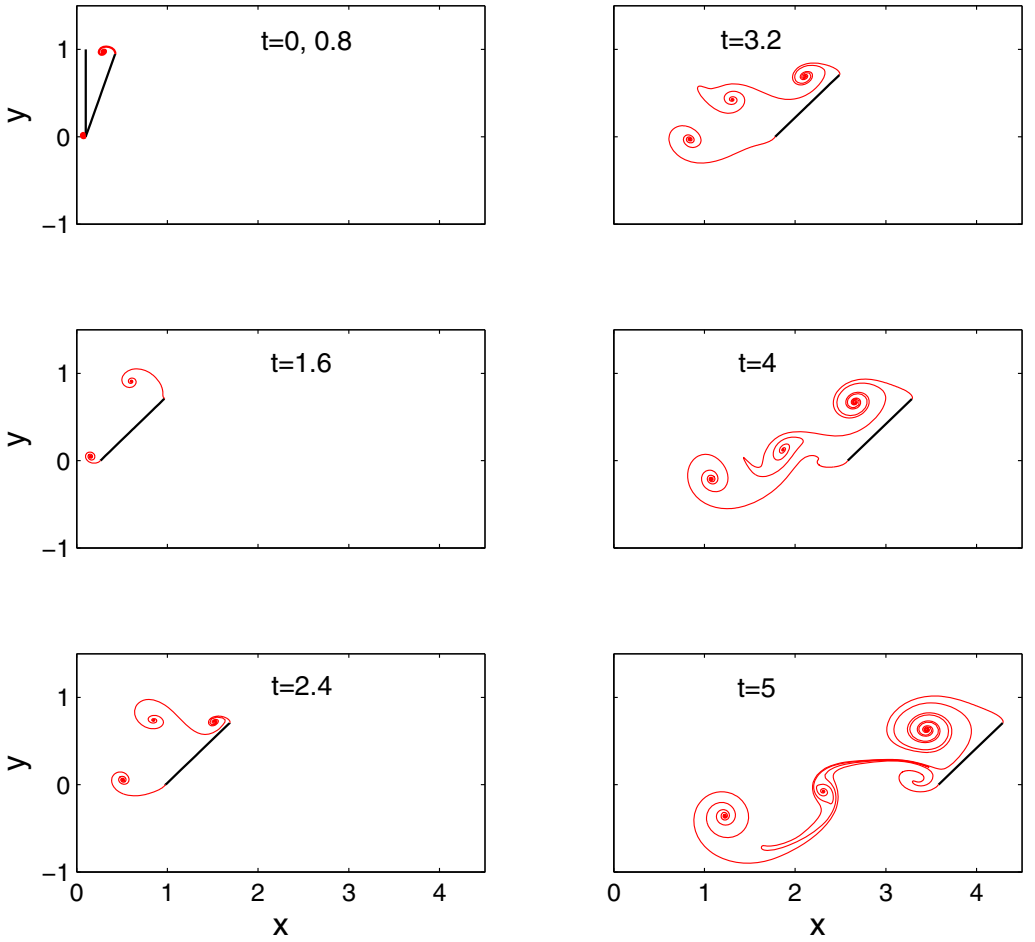


FIG. 11. Vortex shedding of the fling motion by one wing.

separated during translation in the one-winged fling, whereas there is no new leading edge vortex in the two-winged fling. (2) At the late translational phase, a new separating vortex at the trailing edge is strong in the two-winged fling, while it is weak in the one-winged fling. From Fig. 14, we conclude that lift by two wings is enhanced at rotational and translational acceleration phases, but not at the constant translational phase, in the inviscid model. Note that for the NS simulation, lift by two wings is larger than that by one wing over all the ranges of the fling stroke.

The mean lift coefficients of one-winged and two-winged flings are compared in Table I. The mean lift coefficients are calculated separately during rotational and translational acceleration and during constant translation. We confirm that

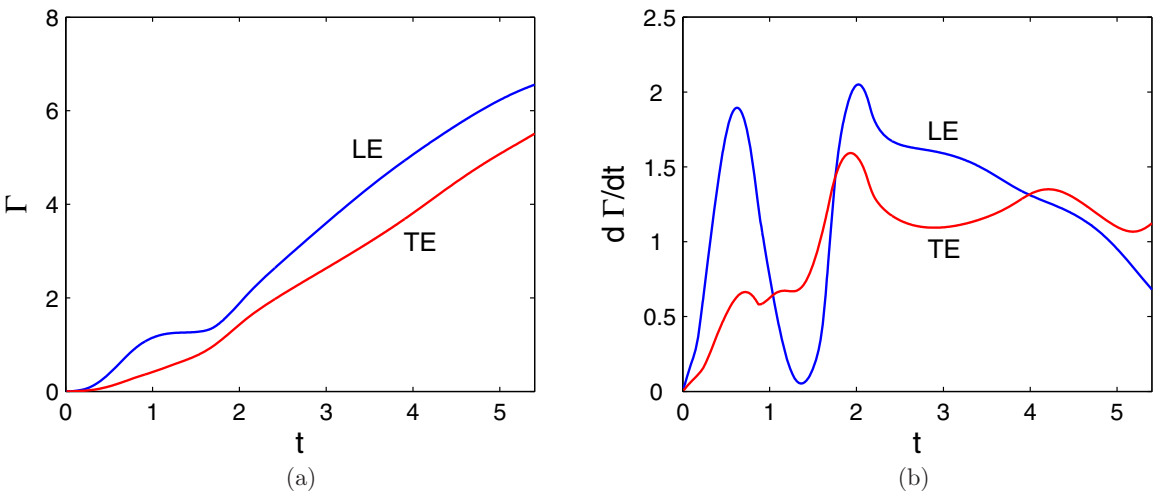


FIG. 12. (a) Circulation and (b) shedding rate at the leading and trailing edges of the fling motion by one wing.

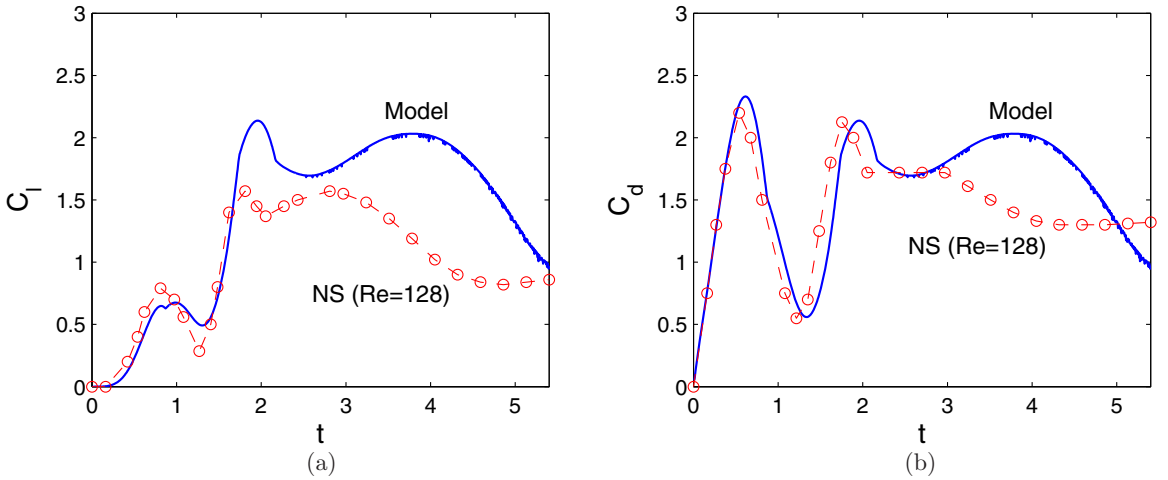


FIG. 13. (a) Lift coefficient and (b) drag coefficient of the fling motion by one wing. The curve is the prediction from the inviscid model, and the circle is the result of the Navier-Stokes simulation for Re = 128.

lift of the two-winged fling is larger than one-winged fling when the wings accelerate and is smaller when they translate. For both of the one-winged and two winged flings, the mean lift coefficient during translation is larger than that during acceleration; however, in the case of one-winged fling, the mean lift differs largely between acceleration and translation, whereas for the two-winged fling, the difference between the two phases is small. Note that the mean lift coefficient over all the time range is 1.36 for the one-winged fling, and 1.27 for the two-winged fling.

We also compare the computational results using different values of the regularization parameter $\delta_0$. Figure 15 shows the vortex shedding of the two-winged fling motion at $t = 2$ and 4 with $\delta_0 = 0.2$ and 0.1. The computation with $\delta_0 = 0.1$ gives more refined solution for the vortex cores. Figure 16 is the comparison of the edge circulation, edge shedding rate, lift coefficient, and drag coefficient for the two-winged fling using $\delta_0 = 0.2$ and 0.1. The thick curves correspond to $\delta_0 = 0.2$, and the thin curves correspond to $\delta_0 = 0.1$. The edge circulations

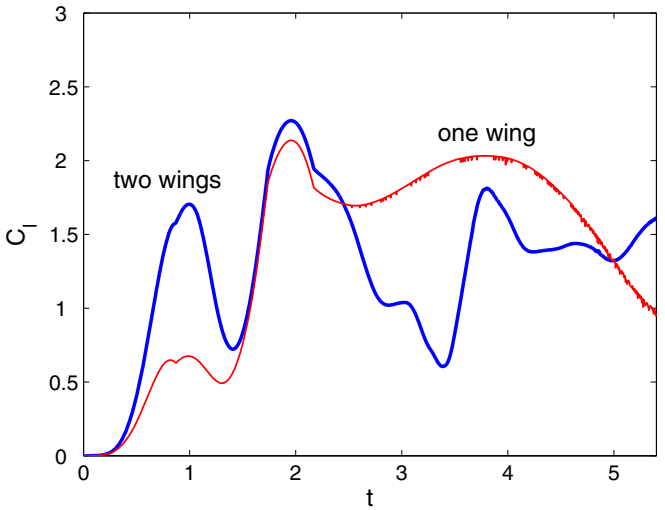


FIG. 14. Comparison of lift coefficients of the one- and two-winged flings.

of the two results are overall in good agreement. The shedding rates at the leading edge of the two results agree well, but some differences are found for the shedding rate at the trailing edge at late times. The second peak of the shedding rate at the trailing edge for $\delta_0 = 0.1$ evolves earlier than that for $\delta_0 = 0.2$, and the shedding rate is oscillatory at late times. The lift and drag are also overall in agreements for the two values of $\delta_0$, but the lift and drag for $\delta_0 = 0.1$ drop faster after $t = 2$ and then increase gradually with oscillations.

## VII. RESULTS FOR CLAP AND FLING

We now present the result for the clap and fling motion. The vortex shedding of clap and fling by two wings is shown in Fig. 17. The regularization parameter is set to $\delta_0 = 0.2$. At $t = 4.5$, the leading edge vortices move ahead of the body as the wings slow down and get close to each other. Remarkably, at $t = 5.4$, the leading edge vortices go away from the wings as the wings clap, due to fluids flowing out of between the wings. We also see this effect at the trailing edge. Then the leading edge vortices fall down and are sucked between the wings as the wings open up. They are highly deformed subsequently and develop to a complex structure. We observe at $t = 6$ that the trailing edge vortices are located very close to the wings, which yield an instability on the computation. These trailing edge vortices move up along the wings. We also see that the trailing edge vortices farthest away from the wings become stronger during the clap stroke, but become weaker during the fling stroke. The streamline of the clap and fling motion at selected times is plotted in Fig. 18, which shows the forward and backward movement of the leading edge vortices.

TABLE I. Mean lift coefficients of one-winged and two-winged flings during acceleration and translation.

| | Acceleration | | Translation | |
|---|---|---|---|---|
| | 1-wing | 2-wings | 1-wing | 2-wings |
| $C_l$ | 0.81 | 1.13 | 1.73 | 1.35 |

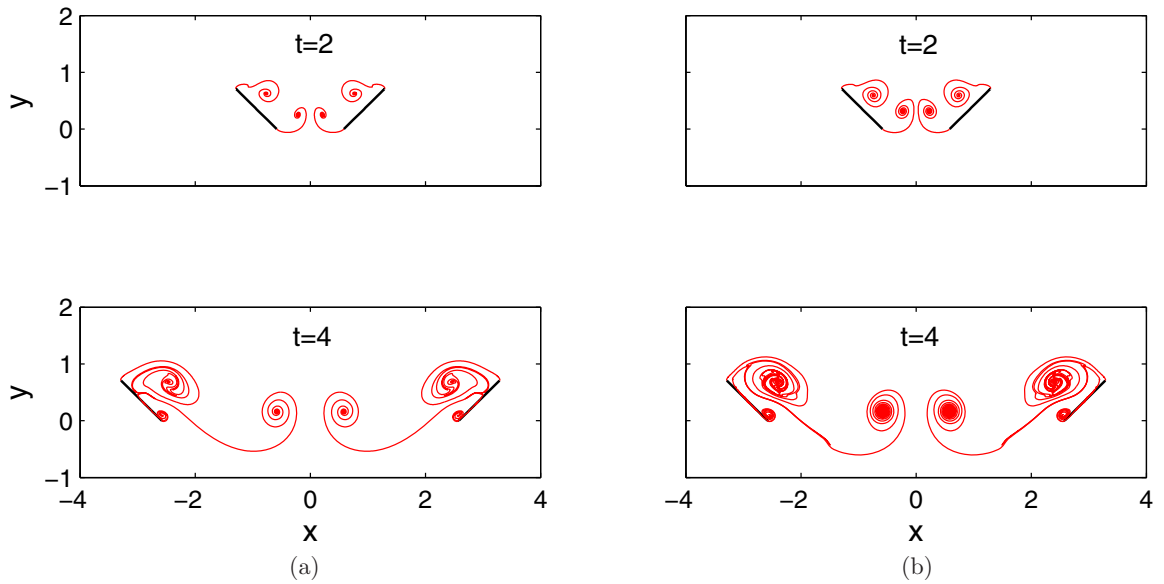


FIG. 15. Comparison of vortex shedding of the two-winged fling at $t = 2$ and 4 with different values of $\delta$: (a) $\delta_0 = 0.2$, (b) $\delta_0 = 0.1$.

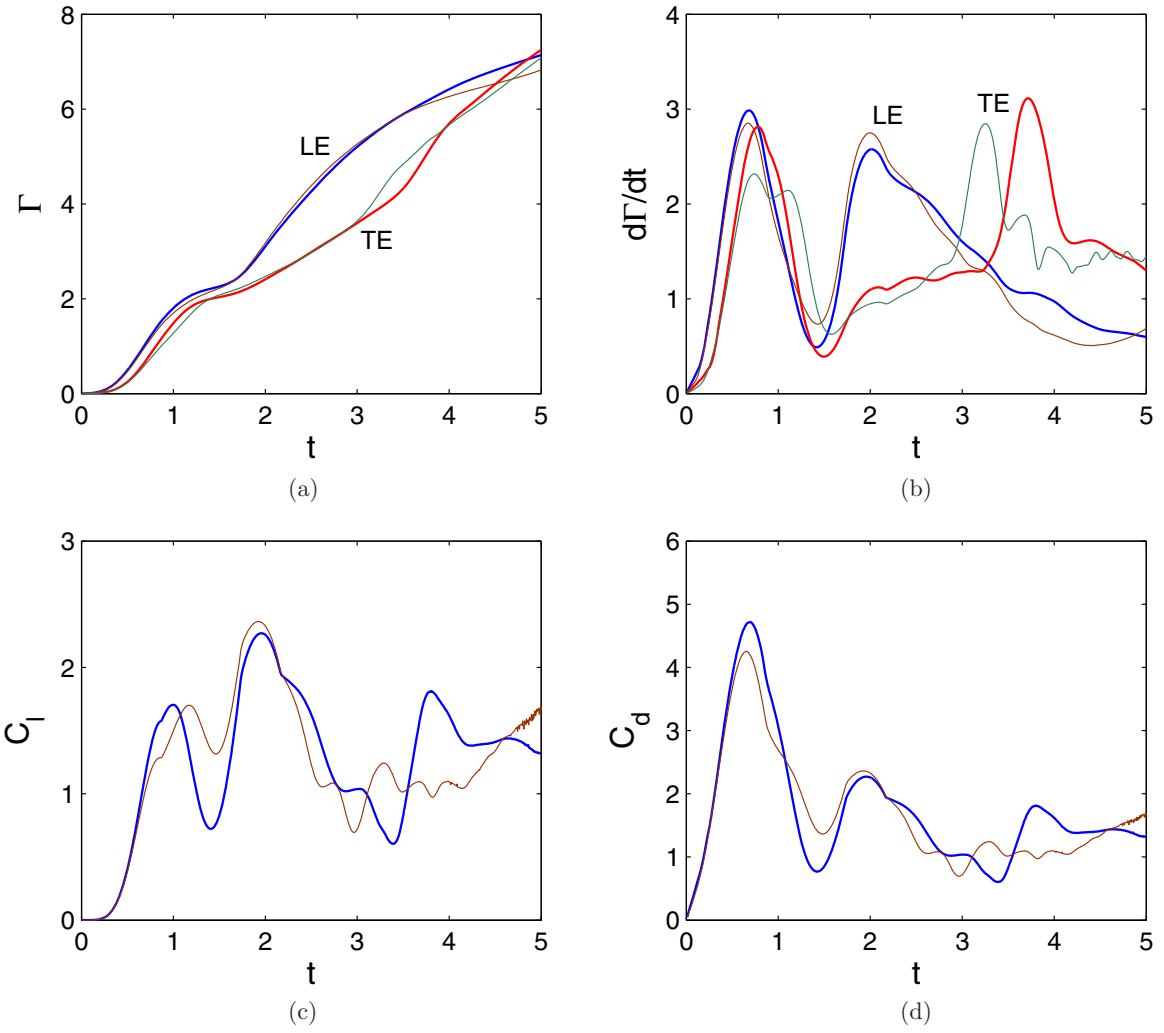


FIG. 16. Comparison of (a) edge circulation, (b) edge shedding rate, (c) lift coefficient, and (d) drag coefficient for the two-winged fling with different values of $\delta_0$. The thick curves (blue and red) correspond to $\delta_0 = 0.2$, and the thin curves (green and brown) correspond to $\delta_0 = 0.1$.

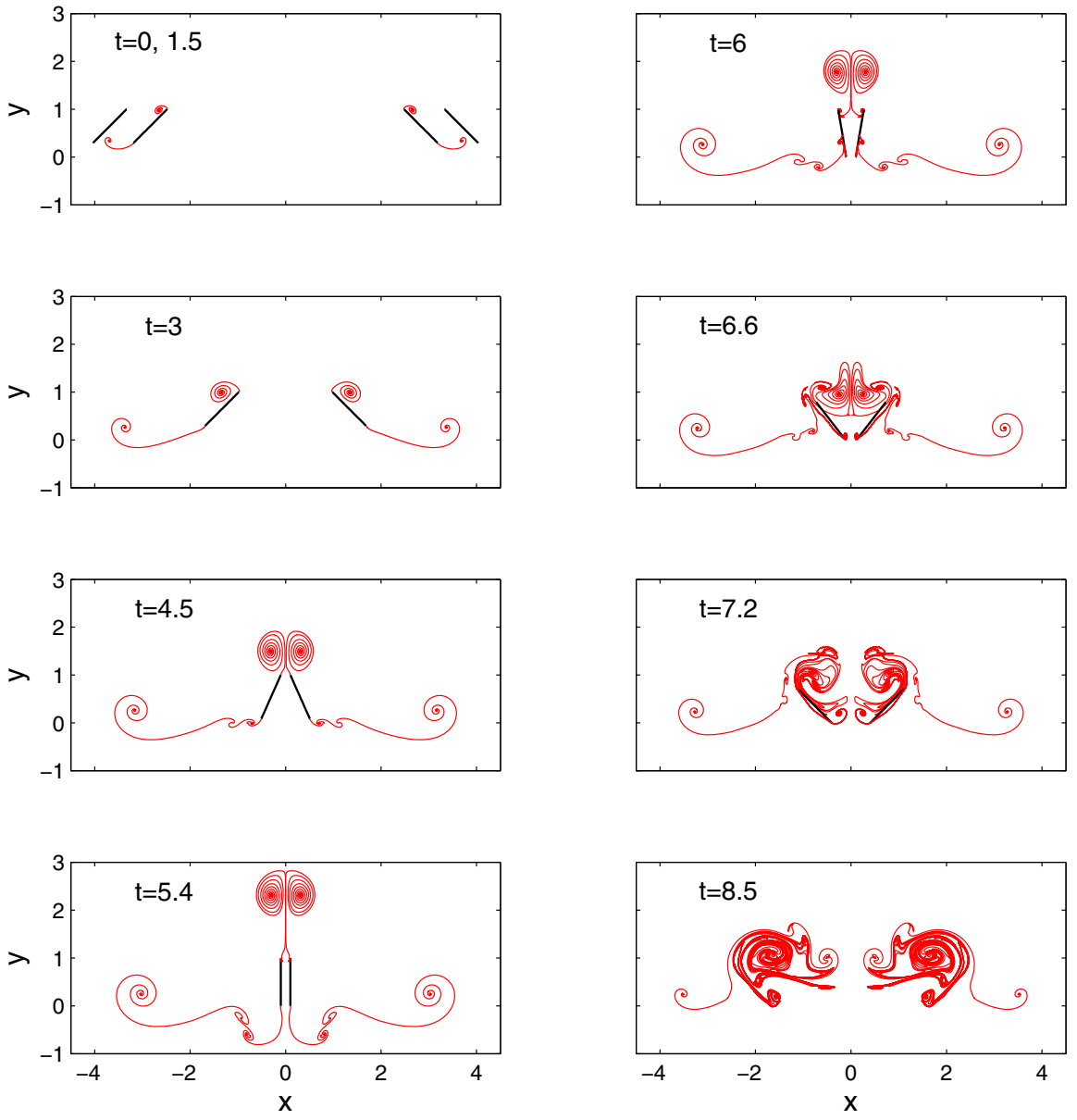


FIG. 17. Vortex shedding of the clap and fling motion by two wings.

As a matter of fact, the condition (31) is not satisfied in the beginning of rotational phase of the fling stroke in the simulation. At this time, the trailing edge vortices are located close to the wings and interact strongly with the wings. Unsatisfaction of the condition (31) yields a numerical instability, but fortunately in this case it does not deteriorate the numerical result severely. The result for the full clap and fling motion could be improved by developing the model.

Figure 19 plots the circulation and shedding rate at the leading and trailing edges. The circulation at the leading edge is larger than that at the trailing edge during translation of the clap stroke, which is similar to the half-fling stroke in Fig. 7. The shedding rates at the two edges are nearly constant during translation of the clap stroke, but at the leading edge it increases greatly after $t = 5.4$ as the wings rotate at the beginning of the fling stroke. The shedding rate, the time derivative of the circulation, shows oscillations at $5.4 < t < 6.4$, especially at the trailing edge, which indicate that the computation tends to be unstable.

Figure 20 shows lift and drag coefficients for the clap and fling motion from the inviscid model and the NS simulation for $\mathrm{Re} = 128$. Lift coefficient increases during translational acceleration in the initial upstroke. Lift coefficient decreases and then gradually increases at $2.5 < t < 3.3$ during translation in the upstroke. Lift drops at $3.3 < t < 4.2$ as the wings decelerate, while it increases in short as the wings begin to rotate. Lift increases after $t > 4.2$ when the wings finish to decelerate, and it becomes nearly zero as the wings get close and clap. Lift dramatically increases after $t = 6$ when the wings rotate at the fling stroke. Another peak of lift coefficient after the highest peak is due to translational acceleration. Lift coefficient drops when the shedding rate at the leading edge goes down and increases again considerably after $t = 8.2$ when the shedding rates at both edges increase. Drag coefficient is

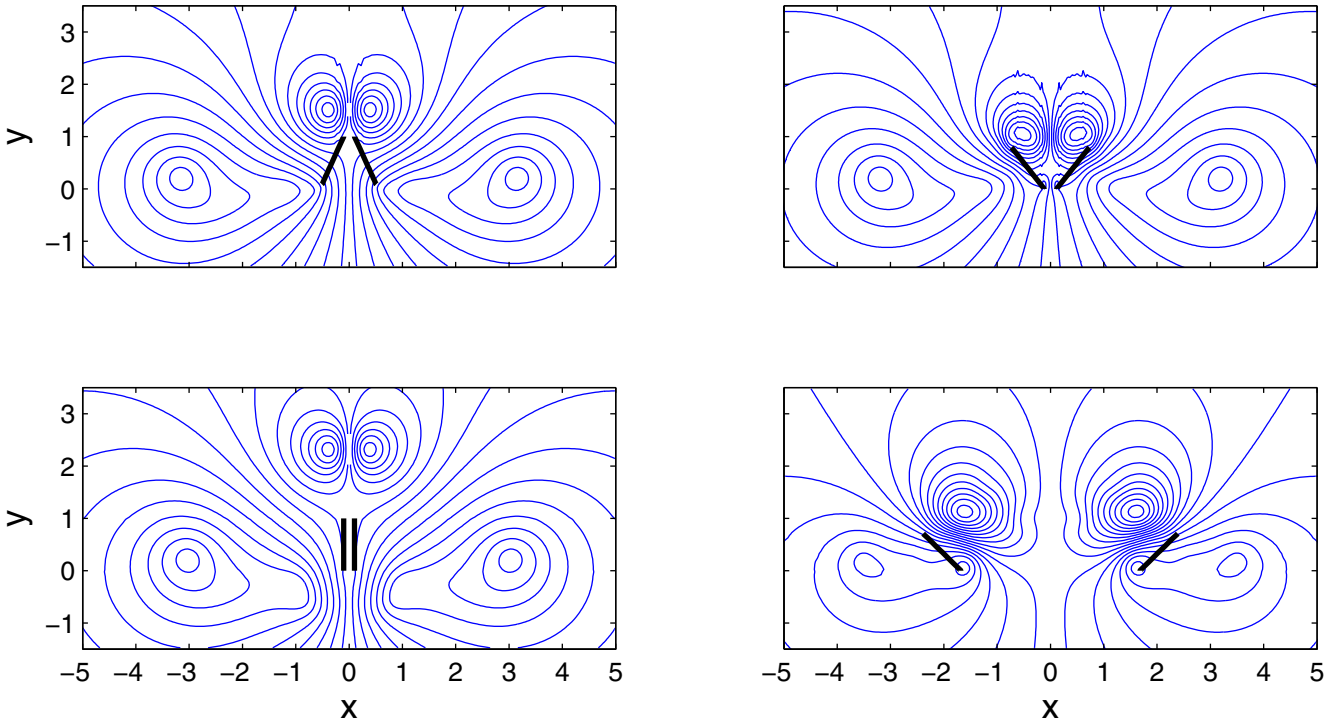


FIG. 18. Streamline of the clap and fling motion by two wings at $t = 4.5$ (upper left), $t = 5.4$ (lower left), $t = 6.6$ (upper right), and $t = 8.5$ (lower right).

similar to the lift coefficient. The lift and drag coefficients of the model are in reasonable agreement with the results of the NS simulation, although the trends of the two results are rather different during both translations of the upstroke and downstroke and at the end of translational deceleration of the upstroke. The drop of lift at $3.9 < t < 4.2$ indicates that the wings lose lift from translational deceleration, in the inviscid model. Importantly, the maximum lift for the inviscid model is twice larger than that for the NS simulation for $\mathrm{Re} = 128$. Note that the maximum lift for $\mathrm{Re} = 128$ is the largest among the results for several values of the Reynolds number considered in Ref. [14].

We also calculate the clap and fling motion by one wing, for comparison with the two-winged motion. Figure 21 shows the vortex shedding of the one-winged clap and fling motion. The leading and trailing edge vortices are formed during translation. The leading edge vortex moves up slightly, and the new trailing edge vortex goes over the wing as the wing slows down and rotates. Then as the wing begins to rotate in the downstroke, the leading edge vortex collides with the wing, and the trailing edge vortex goes back to the right. During translation of the downstroke, the leading edge vortex moves to the left and the flow forms a complicated structure.

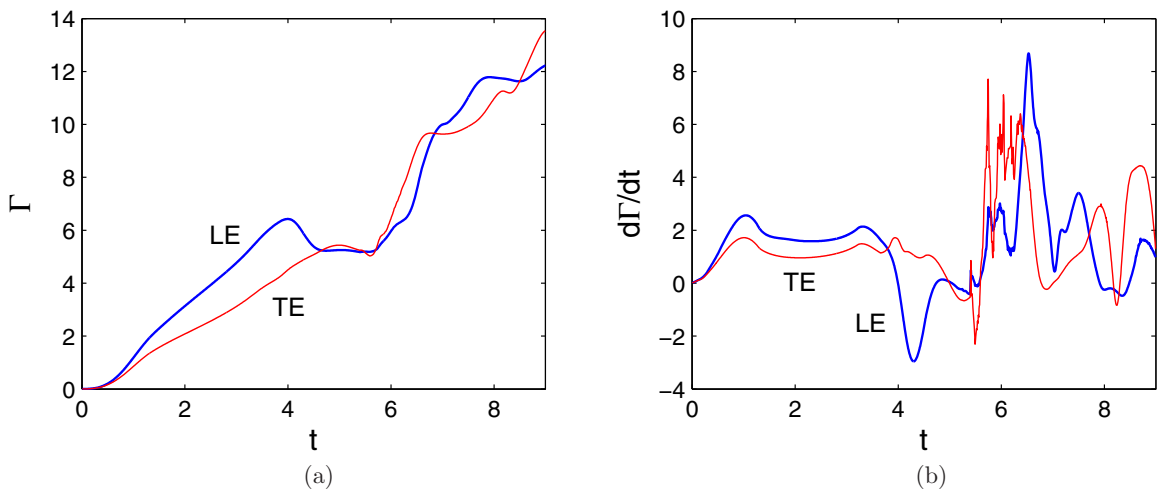


FIG. 19. (a) Circulation and (b) shedding rate at the leading and trailing edges of the clap and fling motion by two wings.

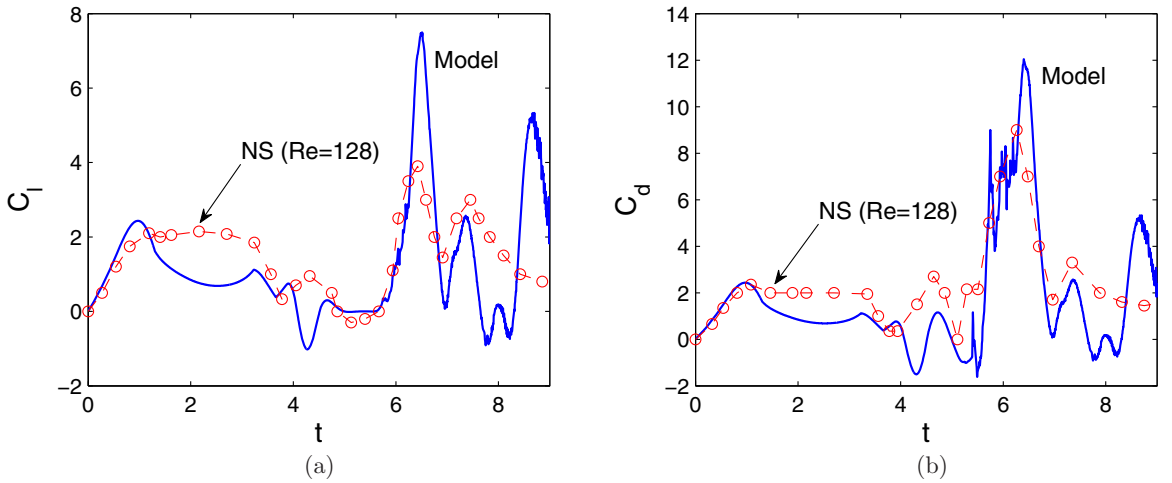


FIG. 20. (a) Lift coefficient and (b) drag coefficient of the clap and fling motion by two wings. The curve is the prediction from the inviscid model, and the circle is the result of the Navier-Stokes simulation for Re = 128.

The circulation and shedding rate at the leading and trailing edges of the one-winged clap and fling motion are plotted in Fig. 22. The edge circulations increase during the translation of the upstroke, but decrease largely as the wing slows down and rotates, and keep decreasing until the wing accelerates in the downstroke, which differ from the two-winged case in Fig. 19. In particular, the leading edge circulation drops steeply at about $t = 6$, in the rotational acceleration phase of the downstroke. The edge circulations increase during translation of the downstroke. The shedding rate also shows a large drop at the leading edge at about $t = 6$. We observe some oscillations on the shedding rate at the leading edge at $5.4 < t < 6.2$, which are caused by the collision of the leading edge vortex with the wing, but are much smaller than those of the two-winged model in Fig. 19.

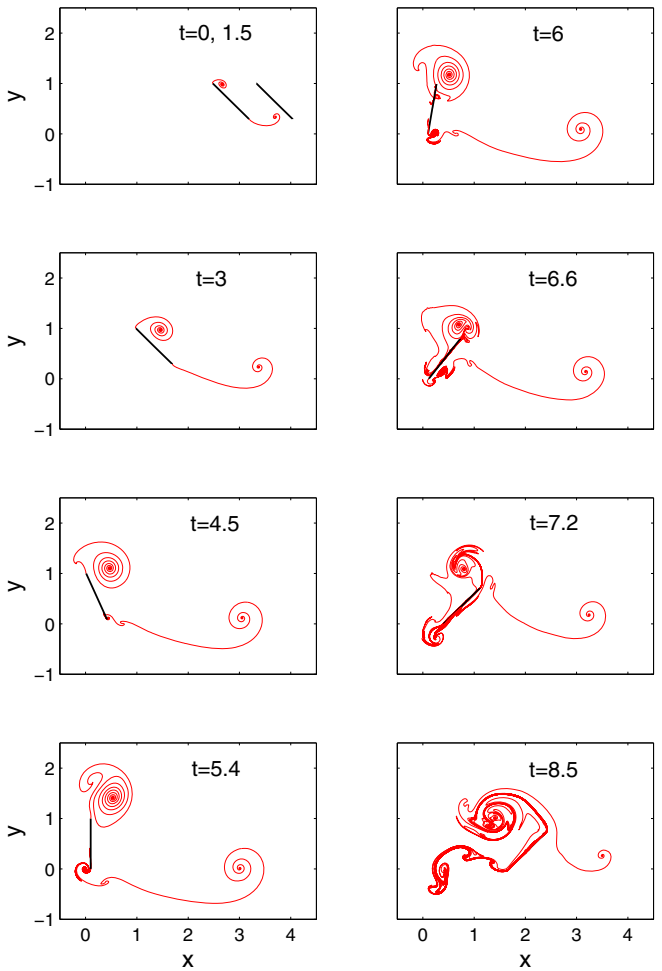


FIG. 21. Vortex shedding of the clap and fling motion by one wing.

Figure 23 shows lift and drag coefficients for the one-winged clap and fling motion from the model and the NS simulation for Re = 128. Lift coefficient exhibits similarly as the two-winged case in the upstroke, but the second peak is comparable to the first peak, unlike the two-winged case. The key difference from the two-winged model is that lift drops to negative at about $t = 6$ when the wing rotates in the downstroke and collides with the leading edge vortex. Lift then increases due to translational acceleration and drops during translation. The lift coefficient of the model is in qualitative agreement with the NS simulation, except the different trends of the two results at about $t = 6$. The drag coefficient mostly varies similarly as the lift coefficient but drops larger to the negative at the end of the upstroke and about $t = 6$. We emphasize that for one wing, lift is lost during rotation of the fling stoke, whereas the two wings generate a large lift at that phase.

## VIII. CONCLUSIONS

We have studied the half-fling and full clap-fling motions of insect flights by applying an inviscid vortex shedding model. The model describes separated vortices at the edges by vortex sheets and has been extended to the two bodies with symmetry. The numerical computations of the model successfully demonstrate sucking of leading edge vortices between the wings in the fling process. Remarkably, it is found that leading edge vortices move forward and backward as the wings close and open in the clap and fling process.

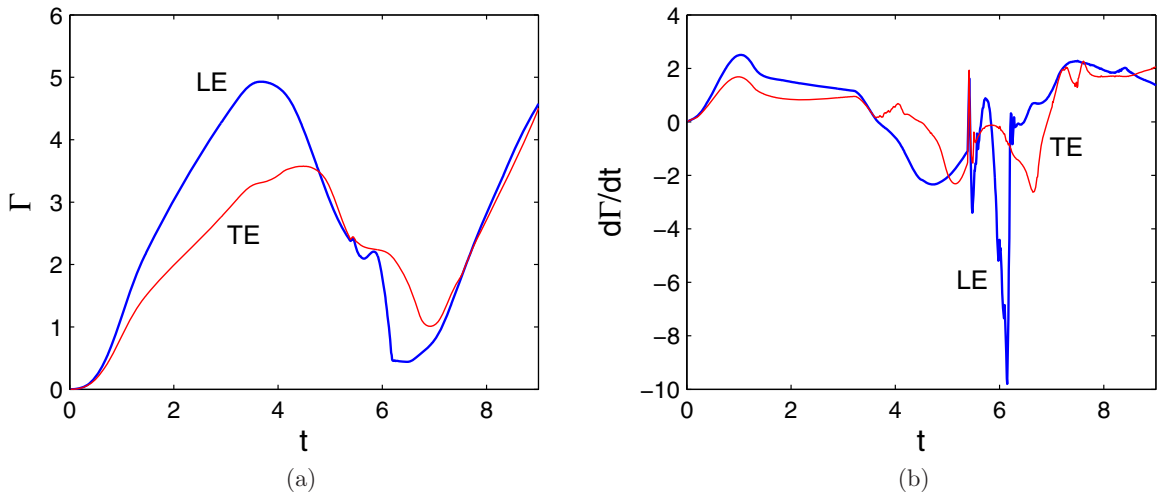


FIG. 22. (a) Circulation and (b) shedding rate at the leading and trailing edges of the clap and fling motion by one wing.

We have also calculated lift and drag coefficients of the wings as well as the edge circulation and shedding rate. The results show that the vortex shedding model describes not only qualitative features but also the quantitative dynamics of the body-vortex interaction. The shedding rates at the edges increase at the rotational and acceleration phases of the fling process, which generate a large lift. Lift of the two-winged fling is much larger than the one-winged fling in the rotational phase, for both the fling-only and full clap and fling strokes.

We have applied the blob regularization method for long-time computation of free vortex sheets. It was shown numerically that the vortex blob model reproduces many features associated with the Navier-Stokes solution with increasing Reynolds number [27], although a direct link of the $\delta$-parameter and the physical effects such as viscosity or layer thickness has not been established yet. Our results indicate an agreement of the model for the flow of moderately large Reynolds numbers $\mathrm{Re} \gtrsim 200$; presumably in the regime of $\mathrm{Re} \sim 1000$.

Maxworthy [9] found that the fling motion for a low and a very high Reynolds number are markedly different. In the experiment of $\mathrm{Re} = 32$, pairs of large leading edge vortices and smaller tailing edge vortices are formed, but for $\mathrm{Re} = 13\,000$, a new pair of leading edge vortices is produced during translation, and trailing edge vortices do *not* appear. This observation indicates that the present modeling may not be valid for very high Reynolds numbers. A possible approach of modeling for the fling motion at a very large Reynolds number is to suppress separation of vortices at the trailing edge. However, validity of this approach should be carefully examined, and we leave it for future study.

The inviscid shedding model shows different characteristics of the clap and fling process from the result of NS simulations. An important finding is that the maximum lift from the inviscid shedding model is considerably larger than the results of the NS simulations for low and moderate Reynolds numbers. This suggests larger instantaneous lift of larger insects than tiny insects. Nonetheless, the lifting force drops during translation

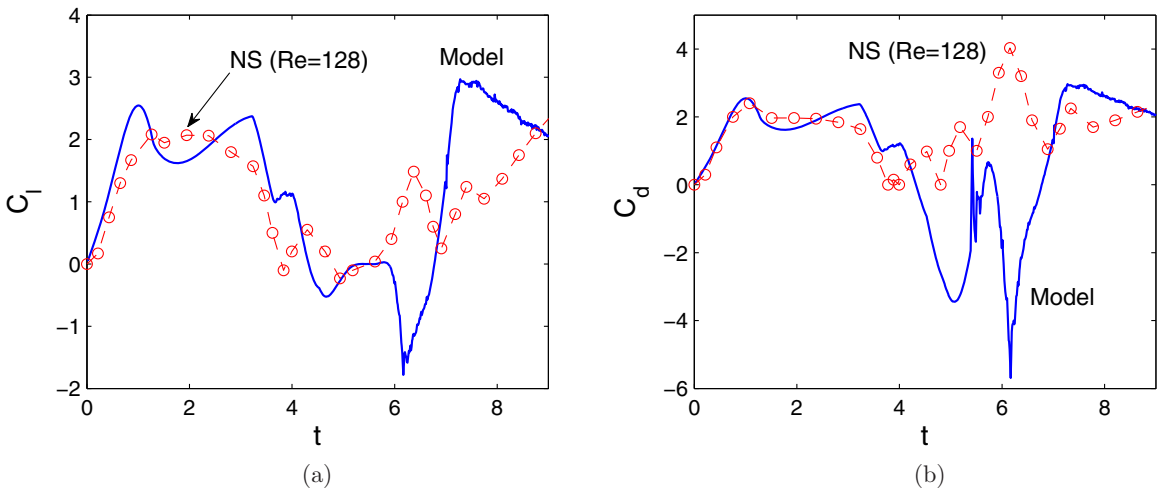


FIG. 23. (a) Lift coefficient and (b) drag coefficient of the clap and fling motion by one wing. The curve is the prediction from the inviscid model, and the circle is the result of the Navier-Stokes simulation for $\mathrm{Re} = 128$.

of wings in the inviscid model, and thus lift enhancement by the Weis-Fogh mechanism will be overall more efficient in small insects flying in low Reynolds numbers.

In our model, the numerical instability appears for a small angle of attack, or close interaction of a free vortex sheet and body, due to nonsatisfaction of the slip condition. A previous method to handle the numerical instability is to turn off the shedding or adjust the velocity of separating vortex points, when the slip condition is not satisfied [17,20]. This technique makes the numerical computation stable but alters the force on the body greatly. In fact, for a small angle of attack, the vortex sheet will separate from the body edge nontangentially, because the velocities above and below the body may have different signs. For complete modeling, this shedding angle should be determined, by introducing a condition. This requires further study of the model.

## ACKNOWLEDGMENTS

This work was supported by the National Research Foundation of Korea (NRF) grant funded by the Korea government (MSIT) under Grant No. NRF-2018R1A2B6002164.

[1] T. Weis-Fogh, J. Exp. Biol. **59**, 169 (1973).
[2] T. Weis-Fogh, Sci. Am. **233**, 80 (1975).
[3] C. P. Ellington, Philos. Trans. R. Soc. B **305**, 41 (1984).
[4] L. A. Miller and C. S. Peskin, J. Exp. Biol. **212**, 3076 (2009).
[5] R. J. Cooter and P. S. Baker, Nature (London) **269**, 53 (1977).
[6] D. W. Murphy, D. Adhikari, D. R. Webster, and J. Yen, J. Exp. Biol. **219**, 535 (2016).
[7] M. J. Lighthill, J. Fluid Mech. **60**, 1 (1973).
[8] L. Bennett, J. Exp. Biol. **69**, 261 (1977).
[9] T. Maxworthy, J. Fluid Mech. **93**, 47 (1979).
[10] G. R. Spedding and T. Maxworthy, J. Fluid Mech. **165**, 247 (1986).
[11] R. H. Edwards and H. K. Cheng, J. Fluid Mech. **120**, 463 (1982).
[12] D. Kolomenskiy, H. K. Moffatt, M. Farge, and K. Schneider, J. Fluid Mech. **676**, 572 (2011).
[13] M. Sun and X. Yu, Acta Mech. Sinica **19**, 103 (2003).
[14] L. A. Miller and C. S. Peskin, J. Exp. Biol. **208**, 195 (2005).
[15] D. Kolomenskiy, H. K. Moffatt, M. Farge, and K. Schneider, J. Fluids Struc. **27**, 784 (2011).
[16] J. M. Birch, W. B. Dickson, and M. H. Dickinson, J. Exp. Biol. **207**, 1063 (2004).
[17] M. Nitsche and R. Krasny, J. Fluid Mech. **276**, 139 (1994).
[18] M. A. Jones, J. Fluid Mech. **496**, 405 (2003).
[19] M. A. Jones and M. J. Shelley, J. Fluid Mech. **540**, 393 (2005).
[20] S. Alben, Phys. Fluids **22**, 061901 (2010).
[21] R. K. Shukla and J. D. Eldredge, Theor. Comput. Fluid Dyn. **21**, 343 (2007).
[22] S. Alben and M. J. Shelley, Phys. Rev. Lett. **100**, 074301 (2008).
[23] D. W. Moore, Proc. R. Soc. London, Ser. A **365**, 105 (1979).
[24] R. Krasny, J. Comput. Phys. **65**, 292 (1986).
[25] S.-I. Sohn, Phys. Fluids **26**, 044105 (2014).
[26] S. Alben, J. Comput. Phys. **228**, 2587 (2009).
[27] G. Tryggvason, W. J. A. Dahm, and K. Sbeih, ASME J. Fluids Eng. **113**, 31 (1991).